

The State-Dependency of Climate Sensitivity and Cloud Responses to CO₂
Doubling

by

Brandon Smith
B.Sc., The Pennsylvania State University, 2019
A Dissertation Submitted in Partial Fulfillment of the
Requirements for the Degree of

MASTER OF SCIENCE

in the Department of Earth and Ocean Sciences

© Brandon Smith, 2023
University of Victoria

All rights reserved. This dissertation may not be reproduced in whole or in part, by photocopying or other means, without the permission of the author.

The State-Dependency of Climate Sensitivity and Cloud Responses to CO₂
Doubling

by

Brandon Smith
B.Sc., The Pennsylvania State University, 2019

Supervisory Committee

Dr. C. Goldblatt, Supervisor
(Department of Earth and Ocean Sciences)

Dr. H. Singh, Committee Member
(Department of Earth and Ocean Sciences)

Dr. A. Monahan, Committee Member
(Department of Earth and Ocean Sciences)

ABSTRACT

Cloud feedbacks are a large source of uncertainty in paleoclimate studies and in the constraint of climate sensitivity, and it is thought that climate sensitivity depends on climate state because of these feedbacks. Here we evaluate the state dependence of both climate sensitivity and cloud responses to CO₂ doubling for a palate of climates with varying solar luminosity and CO₂ concentrations, yet near-equivalent global mean surface temperatures. We find that cloud responses to CO₂ doubling and climate sensitivity are largely dependent on the magnitude of radiative forcing from doubling CO₂ alone, and are therefore independent of climate state. We also determine that the most important responses in clouds occur in the mid-latitude storm tracks, owing to inhibited baroclinic activity as a consequence of a more equable climate under higher CO₂ concentrations.

Contents

| | |
|--|------|
| Supervisory Committee | ii |
| Abstract | iii |
| Table of Contents | iv |
| List of Figures | vi |
| Acknowledgements | vii |
| Dedication | viii |
| 1 Introduction | 1 |
| 2 Experimental Methods | 4 |
| 2.1 Experimental Design | 4 |
| 2.2 How Results Are Calculated | 7 |
| 2.2.1 Circulation | 8 |
| 2.2.2 Cloud Forcing | 8 |
| 2.2.3 Estimated Inversion Strength | 9 |
| 2.2.4 Poleward Heat Transport | 9 |
| 2.2.5 Cloud Droplet Radius (Figure 2.12) | 10 |
| 3 Results | 11 |
| 3.1 Radiative Forcing | 11 |
| 3.2 Comparison of Baseline Climatology | 13 |
| 3.3 Temperature and Circulation | 17 |
| 3.3.1 Climate Sensitivity | 17 |
| 3.3.2 Circulation | 17 |
| 3.3.3 Heat Transport | 18 |

| | | |
|----------|--|-----------|
| 3.4 | Low Clouds | 24 |
| 3.5 | High Clouds | 34 |
| 3.6 | Cloud Microphysics | 38 |
| 3.7 | Global Mean Response of Clouds | 40 |
| 4 | Discussion | 45 |
| 4.1 | Conclusion | 45 |
| 4.2 | Caveats and Shortcomings | 47 |
| 4.3 | Applications | 48 |
| | Bibliography | 50 |

List of Figures

| | |
|--|----|
| Figure 2.1 CESM Workflow | 5 |
| Figure 3.1 Radiative Forcing | 12 |
| Figure 3.2 Background Climate State Vertical Profiles | 15 |
| Figure 3.3 Background Climate State Mapped Variables | 16 |
| Figure 3.4 Climate Sensitivity | 18 |
| Figure 3.5 Surface Temperature Response | 19 |
| Figure 3.6 Stream-function Response | 20 |
| Figure 3.7 Vertical Velocity Response | 21 |
| Figure 3.8 Poleward Heat Transport Response | 23 |
| Figure 3.9 Zonal Mean Cloud Fraction Response | 25 |
| Figure 3.10 Low Cloud Fraction Response | 26 |
| Figure 3.11 EIS Response | 27 |
| Figure 3.12 EKE Response | 28 |
| Figure 3.13 Low Cloud - EKE Regression | 29 |
| Figure 3.14 Seasonal Arctic Ice and Cloud Response | 30 |
| Figure 3.15 Arctic Ice and Cloud Response | 31 |
| Figure 3.16 Antarctic Ice and Cloud Response | 32 |
| Figure 3.17 Zonal Mean Shortwave Cloud Forcing | 33 |
| Figure 3.18 High Cloud Fraction Response | 35 |
| Figure 3.19 Sea Surface Temperature Response | 36 |
| Figure 3.20 Zonal Mean Longwave Cloud Forcing | 37 |
| Figure 3.21 Cloud Water Path | 39 |
| Figure 3.22 Cloud Droplet Radius | 40 |
| Figure 3.23 Cloud Condensation Nuclei | 41 |
| Figure 3.24 Global Mean Cloud Radiative Forcing Response | 42 |
| Figure 3.25 Cloud Radiative Forcing Contributions | 42 |
| Figure 3.26 Zonal Mean Net Cloud Forcing | 44 |

ACKNOWLEDGEMENTS

I would like to first thank my supervisor, Dr. Colin Goldblatt, for his support and guidance through my work on this thesis, and for also mentoring me through my graduate school career. I would like to extend equivalent thanks to Dr. Hansi Singh, who stepped in and assumed supervisory duties while Dr. Goldblatt was incapacitated. I would like to thank Victoria McDonald, who's prior work was foundational for this study, and who offered me guidance and assistance in learning the skills necessary to employ the methodology herein, without which I would be comparable to a fish out of water. I would also like to thank my peers within my research group, and within the School of Earth and Ocean Sciences, for their support and camaraderie during my studies.

Financial support for this research was provided by the Natural Sciences and Engineering Research Council of Canada (NSERC) through Discovery Grant RGPIN-2018-05929, the Canadian Space Agency through FAST Grant 18FAVICB21, and a University Graduate Award from the University of Victoria Faculty of Graduate Studies. High Performance computing resources were provided through NSERC and Research Tools and Equipment Grant RTI-2020-00277, and the BC DRI group and the Digital Research Alliance of Canada (<https://alliancecan.ca/en>).

If I have seen further, it is by standing on the shoulders of giants.

Isaac Newton

DEDICATION

For my Father, the late Col. Graham H. Smith Jr, from whose standard, set in life,
I model my work and my integrity.

Chapter 1

Introduction

The question of how clouds respond to changes in radiative forcing, and how these responses vary depending on background climate state, is an outstanding problem in the realm of paleoclimate and modern climate studies. Clouds are an important and highly nuanced component of the climate system. They impose a radiative forcing in Earth's climate by reflecting solar radiation to space, as well as trapping infrared radiation emitted by the Earth and atmosphere. Incidentally, they are also affected by changes in radiative forcing from other sources such as greenhouse gasses or solar insolation. This simultaneous influence and dependence on the Earth's radiation budget leads to complex, nonlinear feedbacks, which are difficult to simulate even in state-of-the-art climate models, and are at the forefront of current climate research [Stephens, 2005] [Middlemas et al., 2019][Middlemas et al., 2020].

To make matters more complicated, clouds and cloud feedbacks are dependent on climate state. A climate's atmospheric characteristics have great influence over how it will respond to radiative forcing perturbations. An example of this is the dependence of climate sensitivity on background climate state. Climate sensitivity is a measure of the global mean surface temperature response to a doubling of CO₂. Currently, it is understood that specific climate sensitivity, defined as the change in temperature per unit radiative forcing in response to CO₂ doubling, increases as the climate warms due to positive cloud feedbacks [Caballero and Huber, 2013] [Hansen et al., 2013]. Because clouds are highly sensitive to changes in atmospheric temperature, their feedbacks adopt this dependence on background climate state.

Understanding this dependence becomes important in the context of paleoclimate problems such as the Faint Young Sun Paradox (FYSP), an idea first conceived by Sagan and Mullen [1972]. Under a dimmer sun early in Earth's history, Earth's

global temperature would have been substantially lower without compensated radiative forcing from another source. The most plausible source for this was additional atmospheric CO₂ [Owen et al., 1979]; however proxy observations for past CO₂ concentrations through paleosols indicate that CO₂ alone was insufficient in compensating for the amount of radiative forcing necessary to limit glaciation to what is observed in the geologic record [Rye et al., 1995] [Sheldon, 2006]. Another mechanism for keeping the Archean Earth warm is therefore required to solve the FYSP.

Changes to clouds are proposed as one mechanism for which the ancient Earth was kept sufficiently warm [Goldblatt and Zahnle, 2011]. Additional warming would be gained by decreasing the reflectivity of optically thick clouds or by increasing the fractional occurrence of cirrus clouds [Charnay et al., 2013] [Goldblatt and Zahnle, 2011]. An increase in tropical high clouds is proposed as a source of warming for the Archean Earth by Rondanelli and Lindzen [2010], through a mechanism described as the “iris” hypothesis by Lindzen et al. [2001]. Rosing et al. [2010] propose that the necessary warming to resolve the FYSP could be reached through reduced low cloud albedo in the Archean Earth, where the lack of continental land mass lead to a reduction in cloud condensation nuclei. These studies find the global mean surface temperature (GMST) of the Archean to be lower than the present day Earth, though, and a true solution to the FYSP requires GMST to be greater than or equal to that of the present [Hartmann and Michelsen, 2002] [Chambers et al., 2002].

Cloud feedbacks could potentially account for the remainder of necessary radiative forcing to keep the Archean Earth warm. Several different types of cloud feedbacks have been proposed in literature that account for a portion of the necessary warming. Jenkins [1993] find that simulating the Archean atmosphere through increasing CO₂, reducing solar insolation, and increasing planetary rotation rate, leads to a reduction in reflective clouds. Charnay et al. [2013] demonstrate that simulating the Archean climate can result in clouds with larger droplets, resulting in less reflective clouds. Goldblatt et al. [2021] find that reflective stratocumulus clouds stabilize Earth’s long term climate, occurring less frequently under climate conditions analogous to the Archean and more-so under a brightening sun. This is due to the relationship between these clouds and the strength of the cloud top inversion, which is largely determined by the temperature of the free troposphere. These studies utilize 3D general circulation models and can resolve cloud feedbacks that depend upon the geometry of the Earth and would otherwise not appear in 1-dimensional radiative convective models (RCM).

There is disagreement among literature as to whether these feedbacks are best

captured for ancient climates in a 1-dimensional RCM versus a 3-dimensional GCM [Jenkins, 1993][Wolf and Toon, 2013] [Le Hir et al., 2014] [Charnay et al., 2013]. RCMs are useful for modeling the climates of the ancient earth and other planets because they rely on fewer model parameter assumptions (e.g. rotation rate, obliquity, atmospheric mass and composition, continental distribution, etc.), which are difficult to constrain in the context of deep paleoclimate [Goldblatt and Zahnle, 2011] and planetary climate studies [Godolt et al., 2016]. Other studies such as Charnay et al. [2020] believe that 1D RCM's omit valuable feedbacks that depend on the spatial distributions of clouds. Spatially resolved cloud feedbacks are important in answering the question of how clouds respond to CO₂ doublings for different climate regimes, and so we use a 3D GCM with the understanding that there may be internal assumptions not completely applicable to climates of the past.

To the end of constraining uncertainty in cloud feedbacks and climate sensitivity for paleoclimate problems such as the Faint Young Sun Paradox, this study attempts to evaluate the climate-state-dependence of cloud responses to CO₂ doubling experiments for climates analogous to the Archean and the future using a 3D GCM, and to describe the physical processes most responsible for observed changes to clouds. First we analyze changes in cloud fractional occurrence and cloud radiative effect for low and high altitude clouds in different latitude bands, and describe the cause for these observed changes based on understood physical responses of the atmosphere to greenhouse gas forcing. We also analyze the response of clouds to radiative forcing from a micro-physical standpoint, where changes to the particles that comprise clouds can have dramatic impacts on their radiative properties. Finally, we evaluate the response of clouds to CO₂ doubling in a global mean context, identifying the processes that are deemed the most influential in altering the Earth's cloud radiative effect.

Chapter 2

Experimental Methods

2.1 Experimental Design

In this experiment we consider four climate states, each with adjusted solar luminosity of 90%, 95%, and 105% of the present state, in addition to modern conditions ($S_0 = 1361.44 \text{ W/m}^2$). Solar luminosity is varied inversely with atmospheric CO₂ concentration so as to maintain a consistent global mean surface temperature (GMST) for each simulated climates' base state. Once this is achieved, each simulation is then performed again, but with their respective CO₂ concentrations doubled and quadrupled.

We use the Community Earth System Model (CESM) version 1.2.2 with Community Atmospheric Model (CAM) 5 atmospheric physics scheme. The models were run on a 1.9 x 2.5 degree horizontal resolution grid and a 30-level hybrid sigma-pressure vertical coordinate. Simulations used the “E_1850_CAM5” climate component set with pre-industrial initial conditions and a slab-ocean, to expedite model spin-up time. Using a fully coupled ocean would require more computing resources than were available. These configurations follow the framework used in Goldblatt et al. [2021], from which the methods for this study are taken. Each simulation runs for 60 years, with the last 30 years being used for the results, so as to omit the spin-up periods in the beginning of each climate simulation where the atmosphere is not radiatively balanced. Spin up periods for each climate simulation are branch runs that stem from a parent run. Climatology runs are continuations of their respective spin-up runs. Figure 2.1 shows how we organized the branching of model runs. Model output was created at increments of one month model run-time and variables that were used

Architecture for Creating Model Output

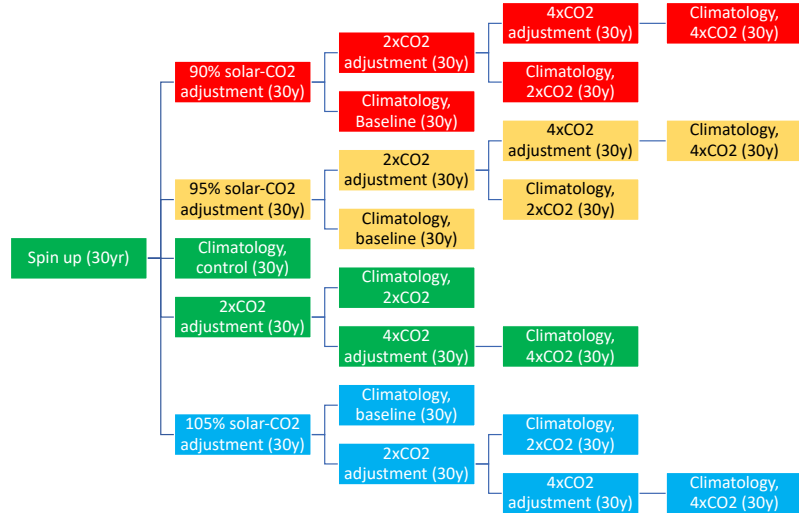


Figure 2.1: workflow chart mapping the continuity of CESM experiments used in this study. Simulations with 90% solar luminosity are red. Simulations with 95% solar luminosity are yellow. Simulations with 100% solar luminosity are green. Simulations with 105% solar luminosity are blue.

in this study are located in table 2.1, comprised of both default variables and manually selected variables. Running CESM at 4xCO₂ and 90% present solar luminosity required reducing the model time step by half, as the climate was rapidly changing.

A tumultuous but necessary stage of this procedure required determining the best CO₂ concentrations to use to maintain a consistent global mean surface temperature across each initial climate state. This was performed by computing the radiative forcing from a given CO₂ concentration that compensated the change in TOA solar flux from adjusted solar luminosity. This keeps the aggregate radiative forcing on the climate, and therefore the GMST, roughly constant. From Byrne and Goldblatt [2014], radiative forcing as a function of CO₂ concentrations follows a polynomial relationship:

$$F_n = 0.39 \ln \left(\frac{C}{C_0} \right)^2 + 5.32 \ln \left(\frac{C}{C_0} \right) \quad (2.1)$$

Where F_n is the radiative forcing inflicted by adding a CO₂ concentration C , and C_0 is a constant of 287ppmv. The value for F_n in this case would be equal and

Table 2.1: List of CESM Model Output Fields and Associated Variables. Gray-highlighted fields are added manually before model execution.

| Fields added to Model Output | | | | |
|------------------------------|------------|---|-------------------|---------------------|
| Variable | Field Name | Long Field Name | Units | Dimensions |
| - | ASDIF | Albedo, Shortwave Diffuse | - | (time,lat,lon) |
| - | ASDIR | Albedo, Shortwave Direct | - | (time,lat,lon) |
| - | CAPE | Convective Available Potential Energy | J/Kg | (time,lat,lon) |
| N_c | CDNUMC | Vertically Integrated Droplet Concentration | m^{-2} | (time,lat,lon) |
| - | CIN | Convective Inhibition | J/Kg | (time,lat,lon) |
| - | CLDHGH | High Cloud Fraction | - | (time,lat,lon) |
| - | CLDLLOW | Low Cloud Fraction | - | (time,lat,lon) |
| - | CLOUD | Total Cloud Fraction | - | (time,lev,lat,lon) |
| - | CONCLD | Convective cloud cover | - | (time,lev,lat,lon) |
| - | FLNS | Net Longwave Flux at Surface | W/m^2 | (time,lat,lon) |
| R_{TOA} | FLNT | Net Longwave Flux at Top of Model | W/m^2 | (time,lat,lon) |
| - | FREQSH | Fractional occurrence of shallow convection | - | (time,lat,lon) |
| - | FSNS | Net Solar Flux at Surface | W/m^2 | (time,lat,lon) |
| R_{TOA} | FSNT | Net Solar Flux at Top of Model | W/m^2 | (time,lat,lon) |
| - | ICIMRTOT | Total in-cloud ice mixing ratio | Kg/Kg | (time,lev,lat,lon) |
| - | ICLMRTOT | Total in-cloud liquid mixing ratio | Kg/Kg | (time,lev,lat,lon) |
| - | LHFLX | Latent Heat Flux | W/m^2 | (time,lat,lon) |
| F_{cloud} | LWCF | Longwave Cloud Forcing | W/m^2 | (time,lat,lon) |
| - | PCLDTOP | Pressure of cloud top | Pa | (time,lat,lon) |
| P | PRECC | Convective Precipitation Rate | m/s | (time,lat,lon) |
| P | PRECL | Large Scale Precipitation Rate | m/s | (time,lat,lon) |
| - | PRECSC | Convective Snow Rate (water equivalent) | m/s | (time,lat,lon) |
| - | PRECSL | Large Scale Snow Rate (water equivalent) | m/s | (time,lat,lon) |
| q_{850} | Q | Specific Humidity | Kg/Kg | (time,lev,lat,lon) |
| - | QFLX | Surface Moisture Flux | W/m^2 | (time,lat,lon) |
| - | QT | Total water mixing ratio | Kg/Kg | (time,lev,lat,lon) |
| - | QTFLX | Total water flux | Kg/Kg | (time,ilev,lat,lon) |
| RH | RELHUM | Relative Humidity | - | (time,lev,lat,lon) |
| - | SHFLX | Sensible Heat Flux | W/m^2 | (time,lat,lon) |
| - | SST | Sea Surface Temperature | K | (time,lat,lon) |
| F_{cloud} | SWCF | Shortwave Cloud Forcing | W/m^2 | (time,lat,lon) |
| T_s | TS | Surface Temperature | K | (time,lat,lon) |
| T | T | Air Temperature | K | (time,lev,lat,lon) |
| M_{cloud} | TGCLDLWP | Total Grid Box Cloud Liquid Water Path | Kg/m ² | (time,lat,lon) |
| - | TREFHT | 2m Air Temperature | K | (time,lat,lon) |
| \bar{u} | U | Zonal Wind | m/s | (time,lev,lat,lon) |
| \bar{v} | V | Meridional Wind | m/s | (time,lev,lat,lon) |
| \bar{u}^2 | UU | Zonal Wind Variance | m^2/s^2 | (time,lev,lat,lon) |
| \bar{v}^2 | VV | Meridional Wind Variance | m^2/s^2 | (time,lev,lat,lon) |
| Z_{850} | Z3 | Geopotential Height (above sea level) | m | (time,lev,lat,lon) |

opposite to the change in TOA solar flux. Initial simulations of 10 years were executed and their latter 5 years used to determine whether the GMST for climates with CO₂ concentrations for this expression were accurate to within 0.1K. Where the GMST was too warm or too cool, adjustments were made by determining the amount of additional radiative forcing needed for the necessary adjustment in GMST, assuming a climate sensitivity parameter of 0.5 K/W/m² [Byrne and Goldblatt, 2014]. The adjustment in radiative forcing for the given differences in GMST are then used in equation 2.1 to determine a change in CO₂ concentration to give to each climate state. This process is repeated until GMST fell to within the desired range of ±0.1K of the control run GMST.

Table 2.2: CESM Trial Run initial configurations

| Trial One | | | |
|-------------------------|-------------------------------|----------------------------|---|
| Solar Constant Fraction | CO ₂ Concentration | Temperature Difference (K) | F _{TOA} Difference ($\frac{W}{m^2}$) |
| 90% | 5975 ppmv | 0.253 | -1.146 |
| 95% | 1390 ppmv | 0.205 | -0.212 |
| S ₀ | 284.7 ppmv | 0 | 0 |
| 105% | 41 ppmv | -0.076 | 1.732 |
| Trial Two | | | |
| Solar Constant Fraction | CO ₂ Concentration | Temperature Difference | F _{TOA} Difference |
| 90% | 5980 ppmv | 0.05 | -0.14 |
| 95% | 1395 ppmv | 0.17 | -0.11 |
| S ₀ | 284.7 ppmv | 0 | 0 |
| 105% | 40.5 ppmv | 0.08 | -0.04 |
| Trial Three | | | |
| Solar Constant Fraction | CO ₂ Concentration | Temperature Difference | F _{TOA} Difference |
| 90% | 5980 ppmv | 0.05 | -0.14 |
| 95% | 1334 ppmv | 0.03 | -0.02 |
| S ₀ | 284.7 ppmv | 0 | 0 |
| 105% | 40.5 ppmv | 0.08 | -0.04 |

2.2 How Results Are Calculated

In this section, we introduce methods for calculating quantities later used in the results. Variables used in equations described in this section can be found in Table 2.1, along with their identifying name in CESM 1.2.2.

2.2.1 Circulation

We analyze atmospheric circulation changes to explain changes to clouds. Meridional mass stream-function is a quantity frequently used to visualize the mean meridional overturning circulation of the atmosphere. Stream-function is computed as Ψ :

$$\Psi = - \int_z v dz \quad (2.2)$$

where v is the mean meridional wind integrated across the model vertical coordinate dz .

Eddy kinetic energy is one of several quantities used to analyze turbulent eddies and baroclinic waves in the atmosphere, separate from the mean flow. It is calculated as κ :

$$\kappa = \frac{1}{2}(\bar{u'^2} + \bar{v'^2}) \quad (2.3)$$

where u', v' are defined as the difference of squares of winds and variances of each component u, v . Over-bars denote monthly averages.

$$\overline{u'^2} = \overline{u^2} - \bar{u}^2 \quad (2.4)$$

2.2.2 Cloud Forcing

Cloud forcing F_{cloud} is broken down into shortwave and longwave components, and is computed internally in CESM as a residual between all-sky net TOA flux and clear-sky net TOA flux:

$$F_{cloud} = F_{allsky} - F_{clearsky} \quad (2.5)$$

A correction for altered solar luminosity must be made for shortwave cloud forcing by dividing it by $\frac{S}{S_0}$, the fraction of the pre-industrial solar constant used for that climate state, since shortwave cloud forcing is dependent on incident shortwave radiation:

$$SWCF_{corrected} = \frac{SWCF}{S} * S_0 \quad (2.6)$$

This corrected value represents what the change in shortwave cloud forcing would be under a sun with present day solar luminosity

2.2.3 Estimated Inversion Strength

Taken from Wood and Bretherton [2006], estimated inversion strength is calculated as ϵ :

$$\epsilon = \theta_{LT} - \Gamma_m^{850}(Z_{700} - Z_{LCL}) \quad (2.7)$$

where θ_{LT} (Lower Tropospheric Stability) is defined as the difference in potential temperature between 700hPa and the surface, Γ_m^{850} is the moist adiabatic lapse rate at 850hPa, Z_{700} is the geopotential height (Z3) of the 700hPa surface, and Z_{LCL} is the lifting condensation level. Γ_m^{850} is defined as:

$$\Gamma_m^{850} = \frac{g}{c_p} \left[1 - \frac{1 + L_v q_{s850} R_a T}{1 - L_v^2 q_{s850} R_v T^2} \right] \quad (2.8)$$

where g is gravitational acceleration, c_p is the specific heat capacity of dry air, L_v is the latent heat of vaporization of water, q_{s850} is the saturation mixing ratio at 850hPa, R_a is the gas constant for dry air, R_v is the gas constant for water vapor, and T is the surface air temperature. Values for physical constants are given in Table 2.3. From Lawrence [2005], LCL is estimated as

$$Z_{LCL} = \left(20 + \frac{T}{5} \right) (100 - RH) \quad (2.9)$$

where RH is the surface relative humidity and T is the surface air temperature in degrees Celsius.

| Values of Physical Constants | |
|------------------------------|---------------------------------|
| g | $9.86 \frac{m}{s^2}$ |
| c_p | $1008 \frac{J}{KgK}$ |
| L_v | $2.25 \times 10^6 \frac{J}{Kg}$ |
| R_v | $461.5 \frac{J}{KgK}$ |
| R_a | $287.053 \frac{J}{KgK}$ |

Table 2.3: Table of constants used in calculations of results and their values

2.2.4 Poleward Heat Transport

Poleward heat transport is calculated for both the atmosphere and ocean, and the atmosphere is separated into latent heat and dry static energy components. Methods

for calculating poleward heat transport are taken from lectures by Brian Rose at the University of Albany, NY [Rose, 2015]. Heat transport \mathcal{H} is calculated as an integral of net TOA radiative imbalances R_{TOA} weighted by area for every grid cell:

$$\mathcal{H} = 2\pi a^2 \int_{-\frac{\pi}{2}}^{\phi} \cos \phi' (R_{TOA} - r_{TOA}) d\phi' \quad (2.10)$$

where a is the radius of the Earth in meters and ϕ is the latitude increment. Here, r_{TOA} is a corrective term to account for TOA flux imbalances that occur due to natural variability in the model. The ocean component \mathcal{H}_o is defined as

$$\mathcal{H}_o = 2\pi a^2 \int_{-\frac{\pi}{2}}^{\phi} \cos \phi' (F_s - f_s) d\phi' \quad (2.11)$$

where F_s is the net upward flux of Energy at the surface, defined as the sum of net radiative, latent heat, sensible, and snowfall heat fluxes at the surface. f_s is a corrective term similar to r_{TOA} . The atmospheric component \mathcal{H}_a is defined as

$$\mathcal{H}_a = 2\pi a^2 \int_{-\frac{\pi}{2}}^{\phi} \cos \phi' [(R_{TOA} - r_{TOA}) - (F_s - f_s)] d\phi' \quad (2.12)$$

The atmosphere component is further divided into the Latent heat component \mathcal{H}_{LH} and the dry static energy component \mathcal{H}_{dse} :

$$\mathcal{H}_{LH} = 2\pi a^2 \int_{-\frac{\pi}{2}}^{\phi} \cos \phi' [E - P] \phi' d\phi' \quad (2.13)$$

$$\mathcal{H}_{dse} = \mathcal{H}_a - \mathcal{H}_{LH} \quad (2.14)$$

Where E is the net surface water flux and P is the net precipitation (convective + synoptic). Dry Static Energy transport is treated as a residual.

2.2.5 Cloud Droplet Radius (Figure 2.12)

Cloud droplet radius is defined as r_c , where M_{cloud} is the column cloud liquid water content, ρ_l is the density of liquid water, and N_c is amount of cloud droplets in a column:

$$r_c = \sqrt[3]{\frac{3}{4} \frac{M_{cloud}}{\pi \rho_l N_c}} \quad (2.15)$$

Chapter 3

Results

3.1 Radiative Forcing

It was found that doubling CO₂ added a different radiative forcing to each climate state, in accordance with equation 2.1. Differences in radiative forcing arise from the variable relationship between radiative forcing and CO₂ concentration determined by the shape of CO₂ absorption lines [Byrne and Goldblatt, 2014]. This is an undesired detail for comparison of each of our climate states because the global mean surface temperature response (and therefore other temperature dependent fields) are consequently different, masking meaningful details of the dependence of clouds on background climate state. To handle this, each Figure in this results section comes in two versions: One figure on top showing the response to CO₂ doubling, and another figure on bottom where the responses are normalized to their respective radiative forcings F_n to show a response to a radiative forcing equivalent to that of a present-day CO₂ doubling, F_0 , calculated for a given variable X as X_n :

$$X_n = X \frac{F_n}{F_0} \quad (3.1)$$

In future work it would be more ideal to instead increase CO₂ to values that give equivalent radiative forcings for each climate state, rather than simply doubling concentrations.

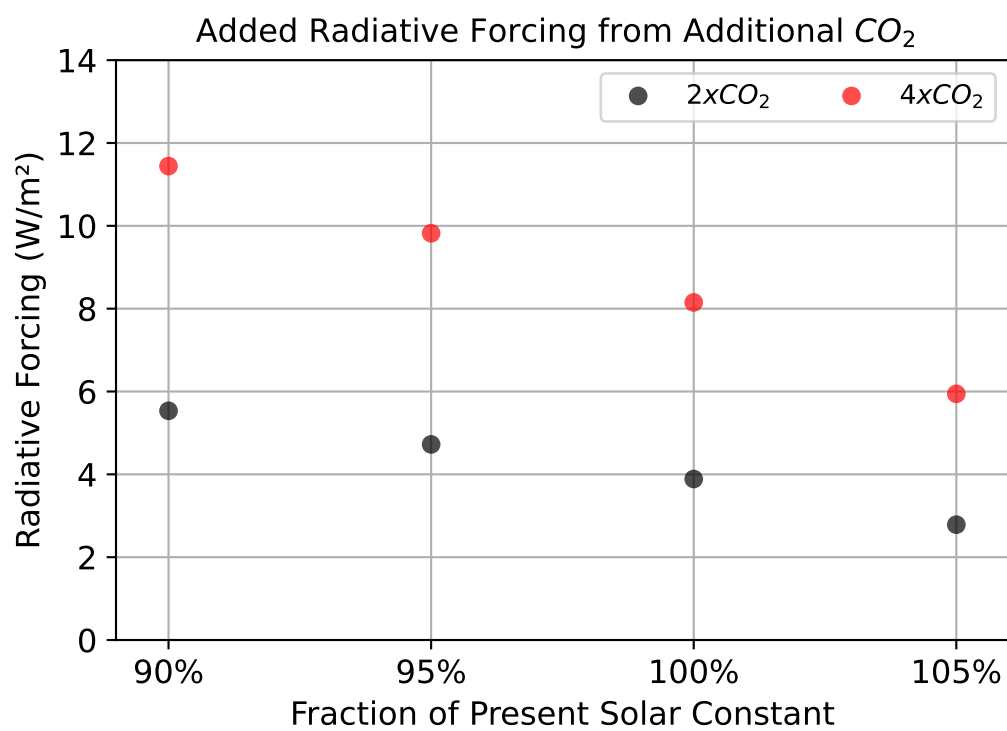


Figure 3.1: Radiative Forcing by CO_2 doublings for each reference climate state, calculated using the fit for CO_2 forcing from table 2 of Byrne and Goldblatt [2014].

3.2 Comparison of Baseline Climatology

As found in prior work, the baseline climatology for each simulation is different, owing to their prescribed solar luminosity and CO₂ concentration. Differences in solar luminosity and CO₂ concentration will affect the heat, moisture and circulation characteristics of each climate state. Climates with a dimmer sun are more analogous to how conditions may have been in the past, whereas climates with a brighter sun are more analogous to how conditions may be in the future. Henceforth, climates with lower solar luminosity and higher CO₂ concentrations will be referred to as early-analog climates, while climates with higher solar luminosity and lower CO₂ concentrations will be referred to as late-analog climates. Figure 3.2 and Figure 3.3 contain a selection of the variables deemed most important for this study. In general, we find that our reference climates are similar to those found in prior work performed by Goldblatt et al. [2021], with the exception of how the mean meridional circulation differs.

Early-analog climates are more equable than late-analog climates; that is their equator-to-pole temperature gradient (EPTG) is weaker. The presence of more greenhouse gas inhibits radiative cooling at the poles, while the dimmer sun reduces the amount of shortwave energy received at the equator. The polar regions and tropical regions of each climate state are consequently warmer and cooler (respectively) for early-analog climates, and vice-versa for late-analog climates. Early-analog climates depict a larger difference in temperature in the Northern hemisphere than the Southern hemisphere with respect to the control climate. At first glance this appears to differ from Goldblatt et al. [2021]; however they primarily represent their findings using results from a Community Atmosphere Model 4 (CAM4) physics scheme. Extended data figures 1 and 2 from their study depict the same results using CAM5, which is the scheme used in this thesis, and show a similar North-South asymmetry in surface temperature. Upper tropospheric and stratospheric temperatures are lower for early-analog climates and higher for late-analog climates, owing to the increased infrared emissions from additional CO₂ molecules. This is a standard result found in Goldblatt et al. [2021].

Low clouds are less prevalent in early-analog climates than they are in late analog climates. This occurs due to processes at the top of the planetary boundary layer, where an inversion allows marine stratocumulus clouds to form. This inversion weakens under higher CO₂ concentrations, allowing drier air from the free troposphere to

mix into the cloud layer and dissipate cloud water [Goldblatt et al., 2021]. Figure 3.3g depicts the reduction in estimated inversion strength that is responsible for the differences in low cloud fraction depicted in Figure 3.3d. The difference in low cloud fraction is globally similar to Figure 5 of Goldblatt et al. [2021], though this experiment demonstrates a stronger dependence on continents and a weaker dependence on subtropical marine stratocumulus layers seen on the western flank of continents.

High clouds are more prevalent under early-analog climate conditions (figure 3.3c). Goldblatt et al. [2021] determined that the cause for the observed greater high cloud fraction is due to a strengthening of the Hadley circulation; this is antithetical to literature on the subject of mean meridional circulation response to increased CO₂, which determine that the Hadley circulation should weaken in response to an increase in CO₂ concentration [Vecchi and Soden, 2007] [Gastineau et al., 2008] [Lau and Kim, 2015] [Feldl and Bordoni, 2016], though these studies do not alter solar luminosity. Additionally, our results do not indicate a clear increase in the strength of the Hadley circulation, but rather a Northward shift (Figure 3.2d). Proposed instead of this idea, more frequent high cloud comes from a higher relative humidity in a cooler upper troposphere, assuming a fixed water mixing ratio, which is observed at high altitudes (figure 3.2c). The observed differences in high cloud fraction are very similar to prior work. Because high clouds have a greenhouse effect that dominates their reflectivity [Goldblatt and Zahnle, 2011], this provides additional longwave cloud forcing that is not observed in late-analog climates.

The total amount of cloud water is lower for early-analog climates than late-analog climates (Figure 3.3d). This is primarily attached to the differences we see in low cloud fractional occurrence. In addition, with a reduced solar insolation, there is less available solar energy to evaporate surface water for early-analog climates, reducing surface latent heat fluxes (Figure 3.3f). Cloud ice is found to be more prevalent for early-analog climates and less so for late analog climates. A cooler troposphere would be more favorable to the formation of ice crystals instead of liquid droplets, and so cloud water for early analog climates is more likely to take the form of ice than liquid water. This supports the observed differences in both cloud liquid and cloud ice for each climate state.

Circulation is affected by differences in radiative forcing parameterization as well. with a weaker EPTG we expect to see weaker Hadley circulations, and vice versa for stronger EPTG [Gastineau et al., 2008]. In our initial climate states, these expected signals are not easily seen. A strong northward shift of the inter-tropical convergence

zone (ITCZ) is seen for early-analog climates, with slight weakening of the southern branch of the Hadley cell, seen in Figure 3.2c. This is related to the hemispheric temperature contrast; because the Northern hemisphere is warmer than the southern hemisphere, the Hadley circulation shifts Northward to transport heat from the Northern to the Southern hemisphere. The late analog climate shows a narrowing of the southern branch of the Hadley circulation, but no overall increases in strength. While the mean tropical circulation does not respond as expected, baroclinic eddies demonstrate an expected behavior. We expect baroclinic eddies to be weaker and less prevalent under a weaker EPTG, owing to thermal wind balance. The transient eddy kinetic energy of the upper tropospheric jet streams (Figure 3.2d) is much weaker under early-analog climates than for late-analog climates. This suggests reduced baroclinic activity in the mid latitudes for early-analog climates, and is an expected result given the more shallow EPTG for these climates.

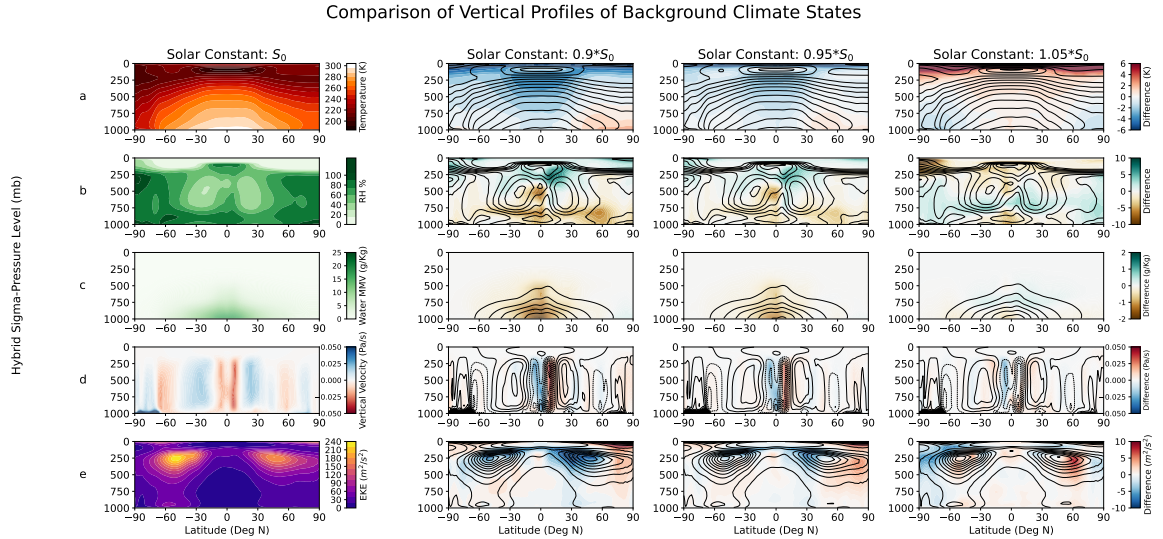


Figure 3.2: Comparison of zonal mean temperature (row 1), relative humidity (row 2), specific humidity (row 3), zonal mean vertical velocity (row 4), and eddy kinetic energy (row 5) for each base climate state. The control simulation is shown in the lefthand column, while differences between each base climate and said control climate are shown in order of ascending solar constant from left to right. For the difference fields, black contours depict the field's raw value, while colors represent the differences with respect to the present day case.

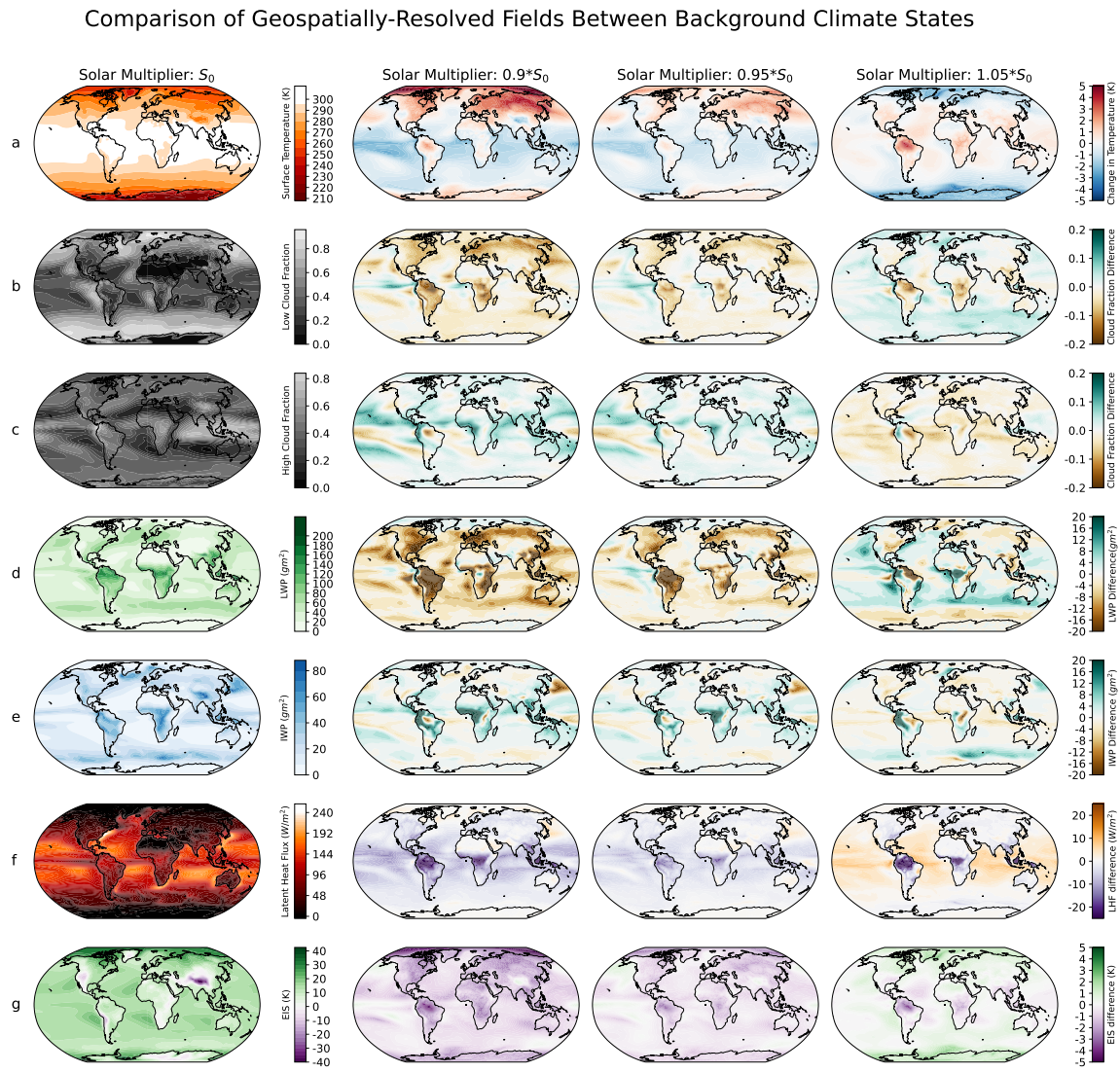


Figure 3.3: From top down, comparison of surface temperature, low cloud fraction, high cloud fraction, cloud liquid water path, cloud ice water path, albedo, and estimated inversion strength for each climate state. The control case is shown in the lefthand column, while differences between each base climatology and the control case are shown in order of ascending solar constant from left to right.

3.3 Temperature and Circulation

Most of the changes in the thermodynamics and dynamics of the climate system due to CO₂ doubling are expected and understood. Polar amplification can be seen in all temperature responses (Figure 3.5). The strength of the meridional overturning circulation is reduced, and this is an expected response. The inter-tropical convergence zone (ITCZ) tends to narrow in response to CO₂ doubling. Both thermodynamic and dynamic changes to the climate affect poleward heat transport for each simulation. Most of the inconsistencies in the responses to CO₂ increase we find across each climate state are from the dynamical response of the atmosphere to CO₂ doubling, particularly with respect to the mean meridional circulation.

3.3.1 Climate Sensitivity

In these experiments it was determined that specific climate sensitivity parameter was remarkably consistent for each simulated climate state. The general consensus in literature is that specific climate sensitivity increases as the climate warms [Yoshimori et al., 2009] [Hansen et al., 2013] [Caballero and Huber, 2013] [von der Heydt and Ashwin, 2016] [Bjordal et al., 2020]; this finding need not apply to this study, however, since we keep the global mean surface temperature consistent for each background climate state. Here we demonstrate that differences in climate sensitivity between background climate state are purely due to differences in radiative forcing from added CO₂ concentrations. We observe a specific climate sensitivity of $1.0 \pm 0.1 K/W/m^2$ for each climate state. It is important to recognize that these differences are negligible in the context of paleoclimate, where climate states are vastly different from present conditions, but not so for anthropogenic climate change studies.

3.3.2 Circulation

Unlike the thermodynamic frame of thinking, the dynamical response to CO₂ doubling is different for each climate state. The mean overturning circulation weakens with solar insolation less than or equal to present day, and is a response agreed upon by current literature [Gastineau et al., 2008][Feldl and Bordoni, 2016]. For the future-analog climate, we instead observe a strong southward shift in the tropical Hadley circulation (Figure 3.6). This is likely in compensation for the fact that sea surface temperatures in the southern hemisphere are anomalously warm. A southward shift

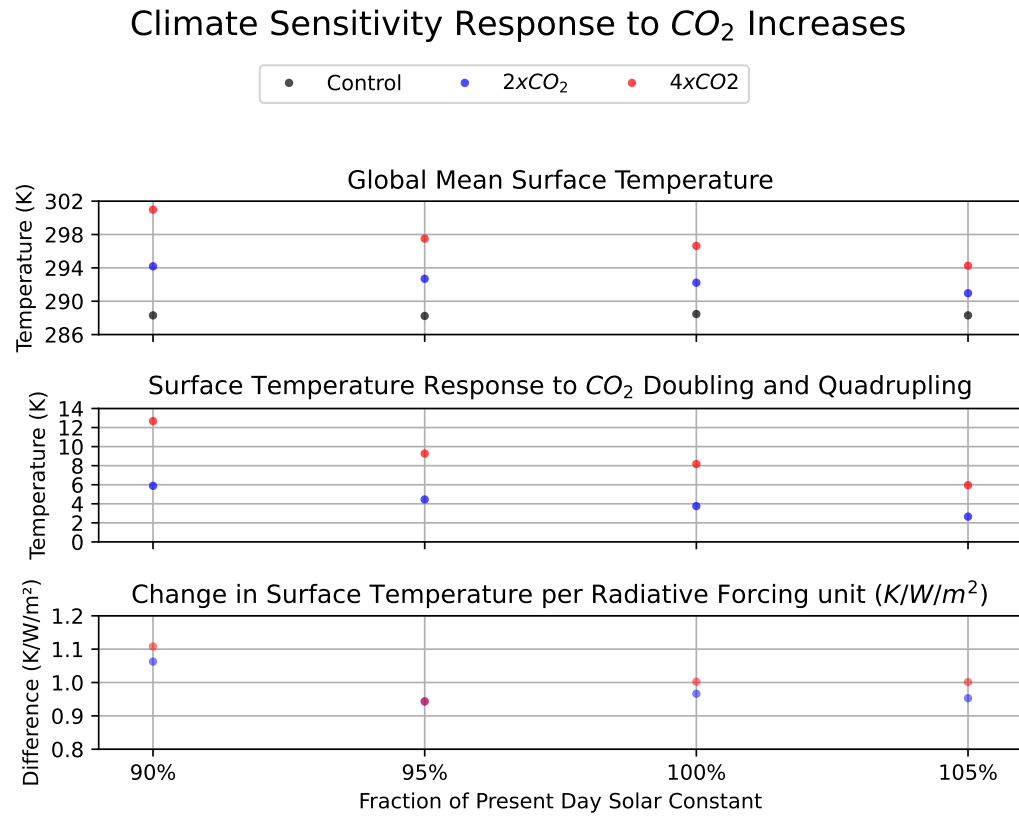


Figure 3.4: Climate Sensitivity response to CO_2 doubling for each climate state. Top: Global mean surface temperature. Middle: Temperature response to CO_2 doubling. Bottom: Temperature response normalized to radiative forcing for each case.

in the ITCZ provides compensatory Northward heat transport to balance this sea surface temperature contrast. The ITCZ appears to contract in response to CO_2 doubling (Figure 3.7). This effect is seen and described by Lau and Kim [2015] as a “deep tropical squeeze”, whereby vertical ascent is stronger at the equator, but weaker along the limbs of the ITCZ. This effect is important for the analysis of high cloud fraction in section 3.5.

3.3.3 Heat Transport

Both the dynamic and thermodynamic response of the climate to CO_2 doubling affect the poleward transport of energy. Figure 3.8 shows how poleward heat transport responds to CO_2 doubling. The most significant changes occur in the transport of latent heat (LHT) and dry static energy (DSET). LHT increases in magnitude under a warmer climate, since warmer air holds more water vapor and can release more latent

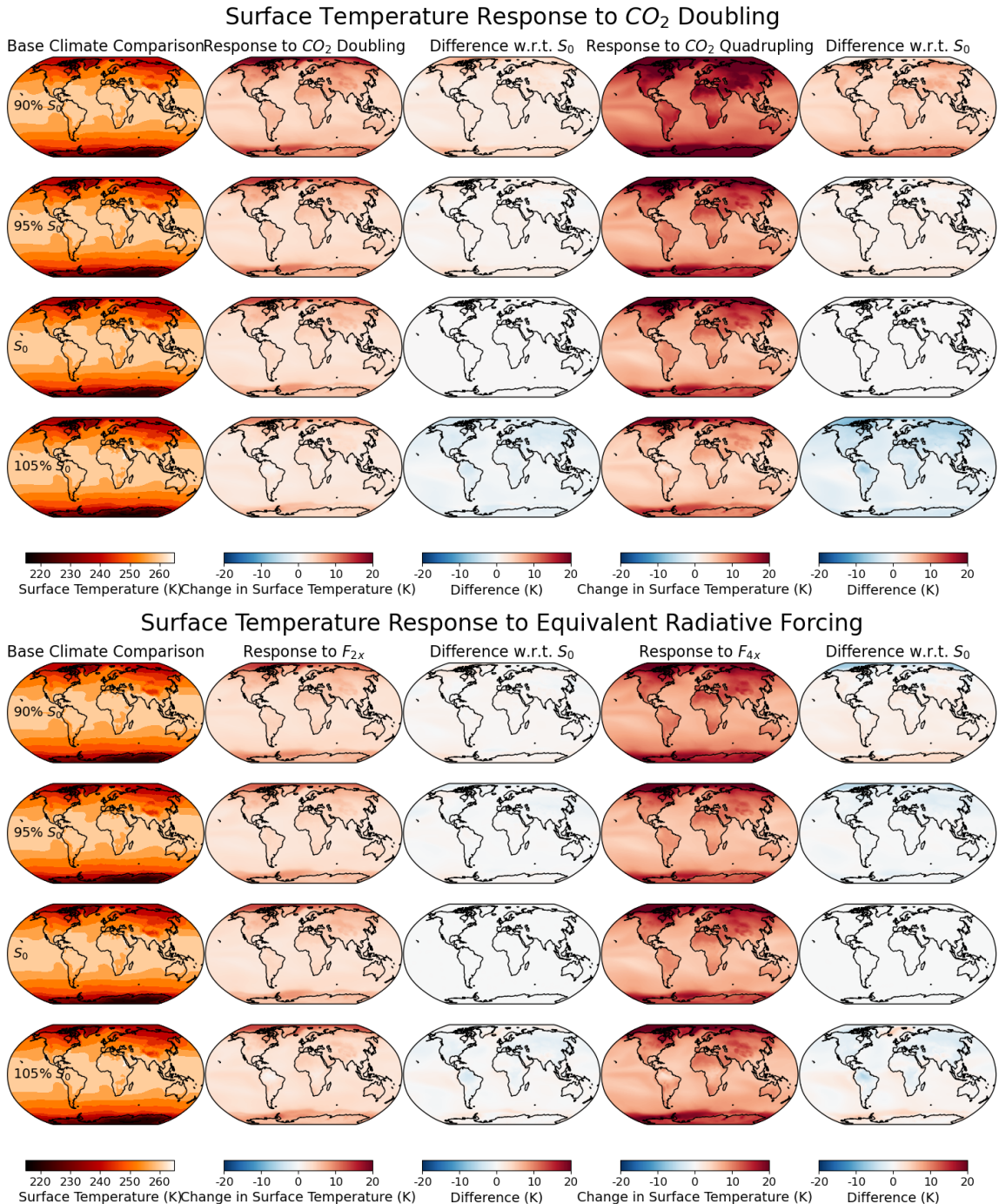


Figure 3.5: Surface temperature Response to added CO₂. Control simulation is shown in the lefthand column, while doubling responses and the difference in response from the modern case are shown from left to right.

heat through condensation. Because LHT is equator ward in the tropics, DSET,

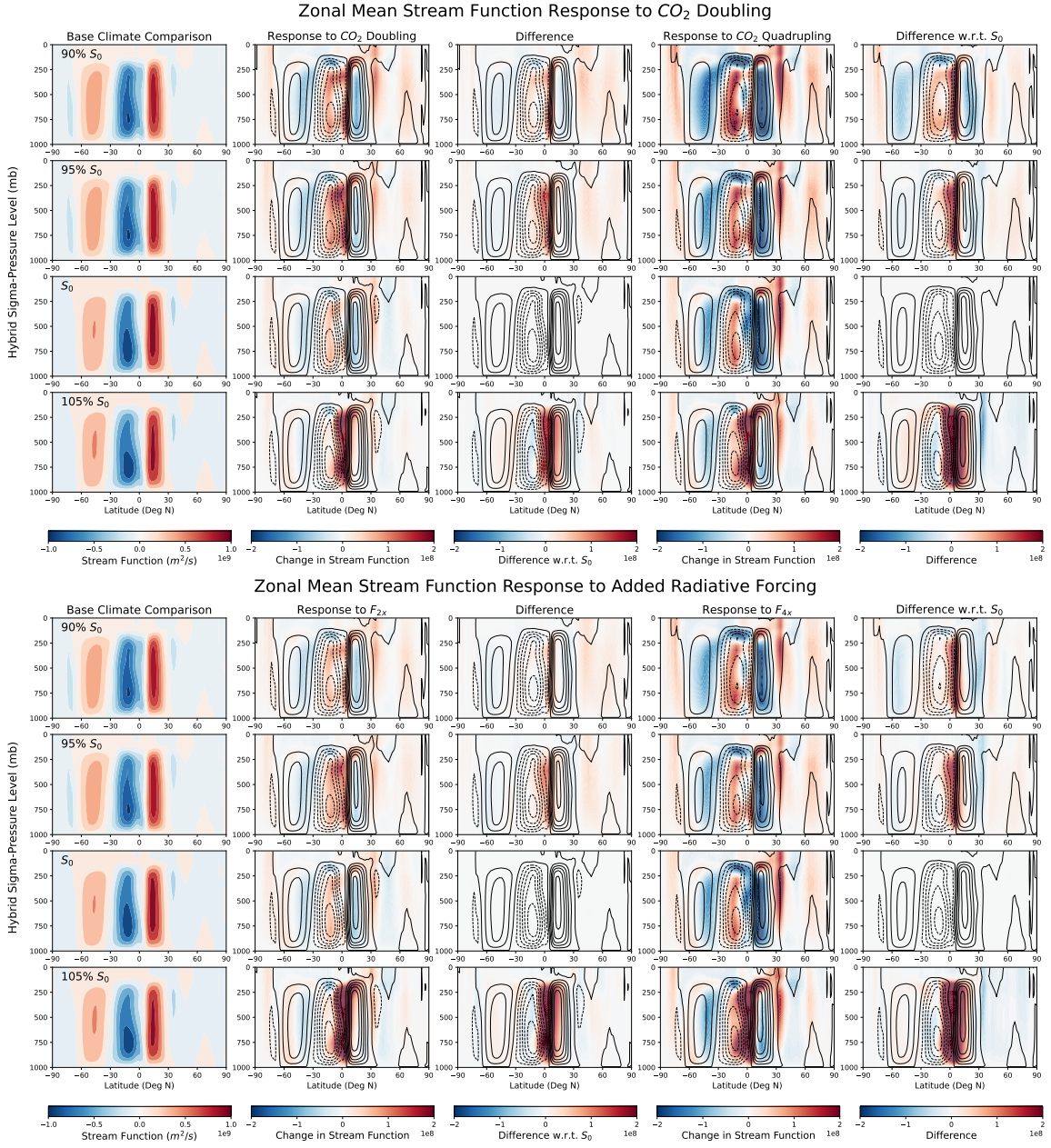


Figure 3.6: Overturning mass-stream-function Response to added CO_2 . Control simulation is shown in the lefthand column, while doubling responses and the difference in response from the modern case are shown from left to right. For the difference fields, black contours depict the field's raw value, while colors represent the differences with respect to the present day case.

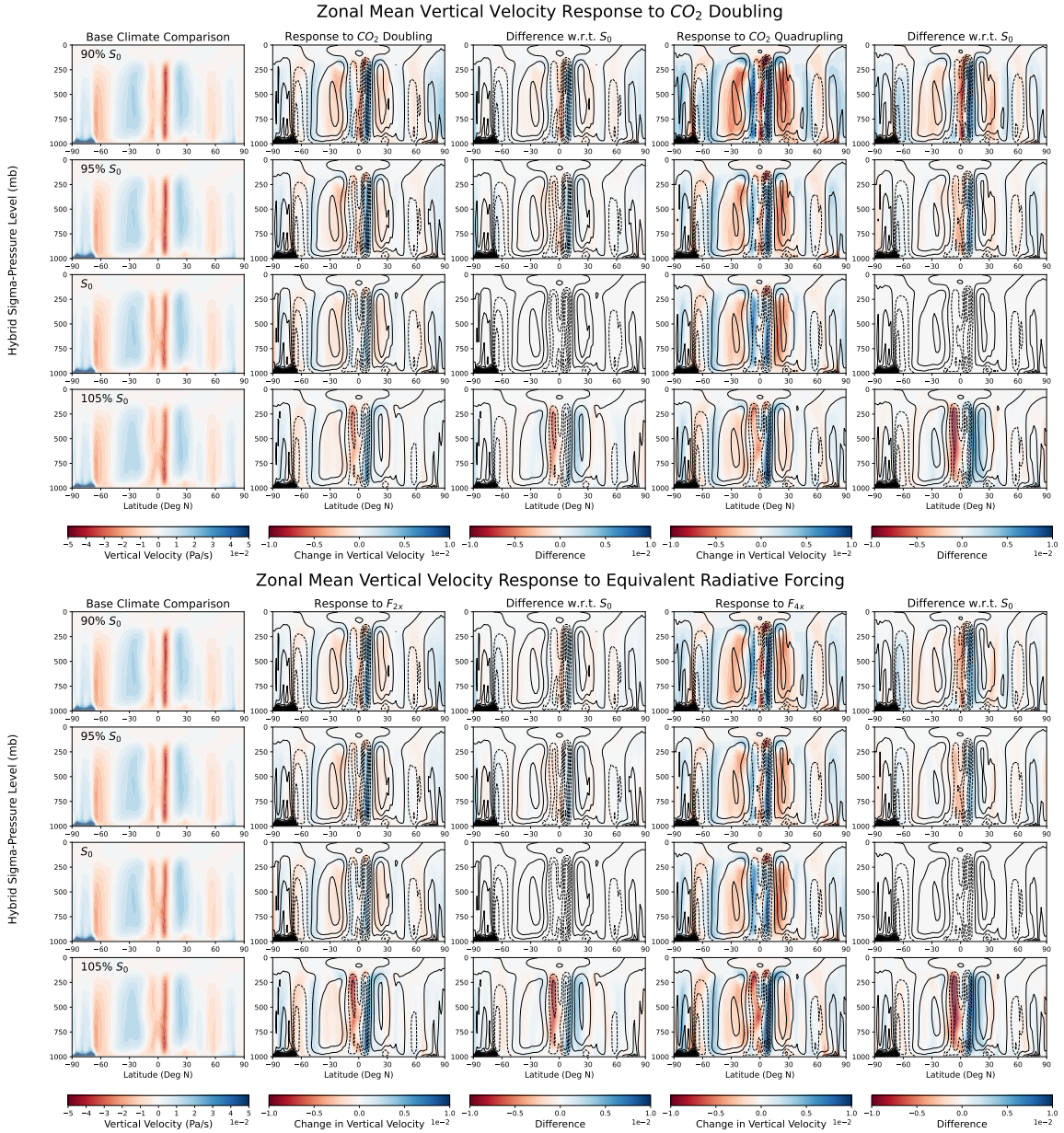


Figure 3.7: Zonal mean vertical velocity response to added CO₂. (increase in) Ascent is red, (decrease in) descent is blue. Control simulation is shown in the lefthand column, while doubling responses and the difference in response from the modern case are shown from left to right. For the difference fields, black contours depict the field's raw value, while colors represent the differences with respect to the present day case.

which is typically poleward in all locations, is found to increase in the tropics. The increase in equator ward flux of heat at the surface is balanced by an increase in poleward flux of heat at the top of the Hadley circulation. This appears as a zone of increased meridional flow between 200hPa and 100hPa (Figure 3.6). The magnitude of this equatorial response is inconsistent across each simulated climate state, seen in Figure 3.8 as opposing spikes in magnitude of either component of the atmospheric transport. For the future-analog climate, we observe an equatorial spike in both DSET and LHT, indicating a Southward shift in the ITCZ in response to CO₂ doubling. In the mid-latitudes, both LHT and DSET are poleward, and a decrease in the strength of the general circulation results in a decrease in DSET. Fundamentally, what we observe in response to CO₂ doubling is a shift in contribution from dry static energy to latent heat as the main carrier of energy transported poleward by the atmosphere.

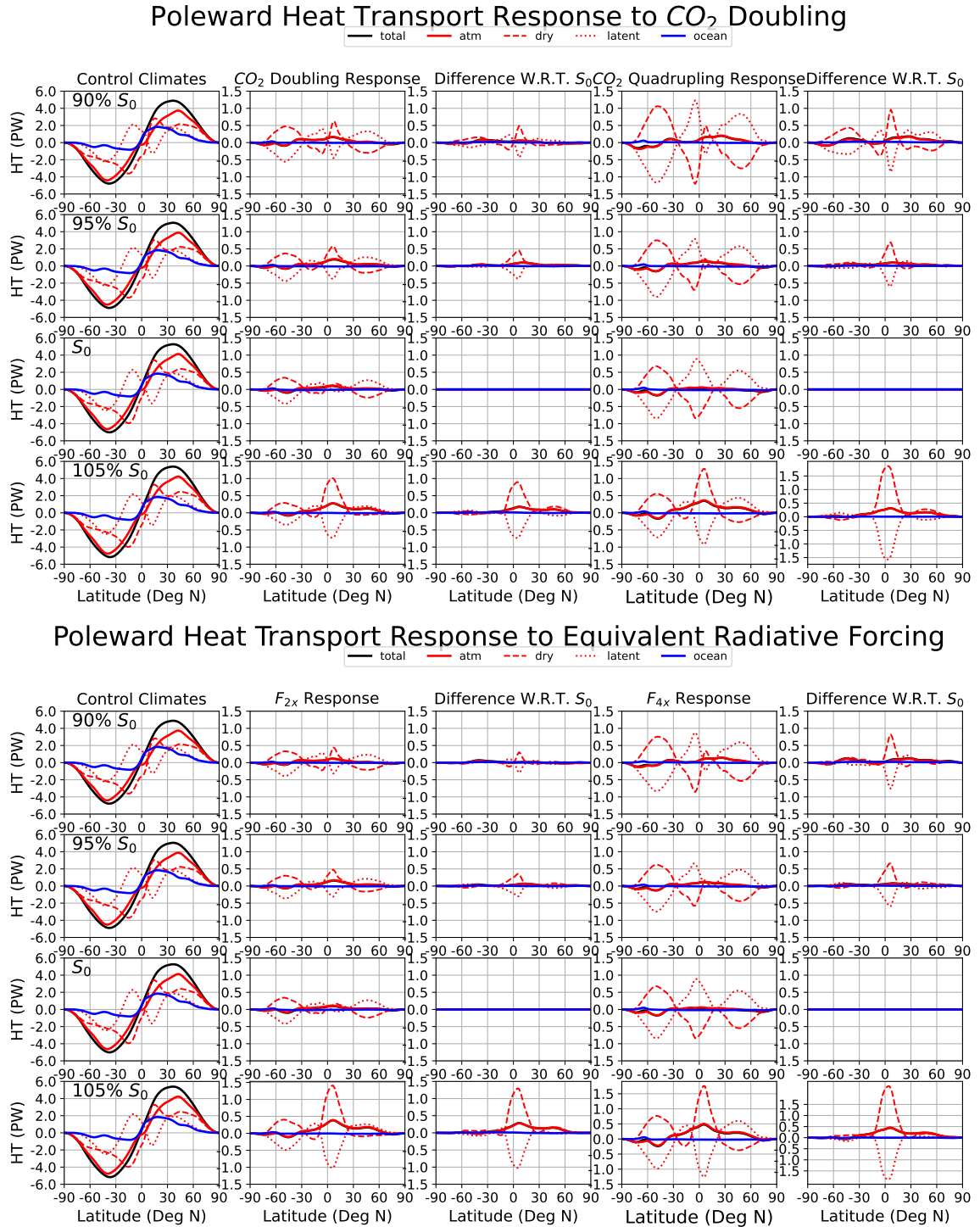


Figure 3.8: poleward heat transport response to added CO_2 , broken down into atmospheric, oceanic, latent heat, and dry static energy components. Values are positive Northward, negative Southward. Control simulation is shown in the lefthand column, while doubling responses and the difference in response from the modern case are shown from left to right.

3.4 Low Clouds

Global reductions in low cloud fraction are seen as the most dominant response to added radiative forcing from CO₂, and are consistent in magnitude for each simulated climate. Figure 3.10 shows the response of low clouds to doubled and quadrupled CO₂ concentrations, as well as the response to equivalent added radiative forcing. The most apparent reductions in low cloud fraction take place over oceans in the mid latitude storm tracks. Low clouds are also less prevalent over continents for early-analog climates, but are more prevalent over continents for late-analog climates. The decrease in low clouds in response to warming over continental tropical regions is less intense for early-analog climates, owing to the difference in the location of the Hadley circulation for these climates. Low clouds are also found to be more prevalent over the arctic and in maritime subtropical regions, particularly so for the early-analog 4xCO₂ case.

Previous comparisons of background climate states in Goldblatt et al. [2021] suggest that absence of low cloud fraction is due to a weakening of the cloud-top inversion in the boundary layer under a cooler free troposphere. The temperature of the free troposphere is largely set by tropical convection, so changes to surface temperature in the tropics are usually representative of changes to free-tropospheric temperature. Systematically weaker inversions can be seen in Figure 3.3g for climates with higher CO₂ concentrations. Because net warming alone occurs under increased CO₂ concentrations, though, we expect and observe increases in the cloud top inversion strength across the majority of the Earth in Figure 3.11 (with the exception of the poles, though in these regions we observe increases in low cloud fraction anyway). Though this is what is likely responsible for the stark increase in low cloud fraction seen in the sub-tropics, we cannot otherwise attribute the reduction in low clouds seen in the mid latitudes to changes in the cloud top inversion in the boundary layer.

Instead, the reductions in low clouds that we observe in the mid latitudes stem from a reduction in atmospheric baroclinicity. The southern ocean is home to strong and consistent mid latitude cyclones year-round, which are a primary source for persistent low clouds. A weaker EPTG reduces the strength of mid-latitude cyclones, maintaining thermal wind balance, and consequently inhibits the formation of low clouds associated with them. This is not to imply causation of changes in clouds by changes in circulation, as both systems are coupled and affect each other, however the correlation between both responses suggests a dependence of changes in clouds

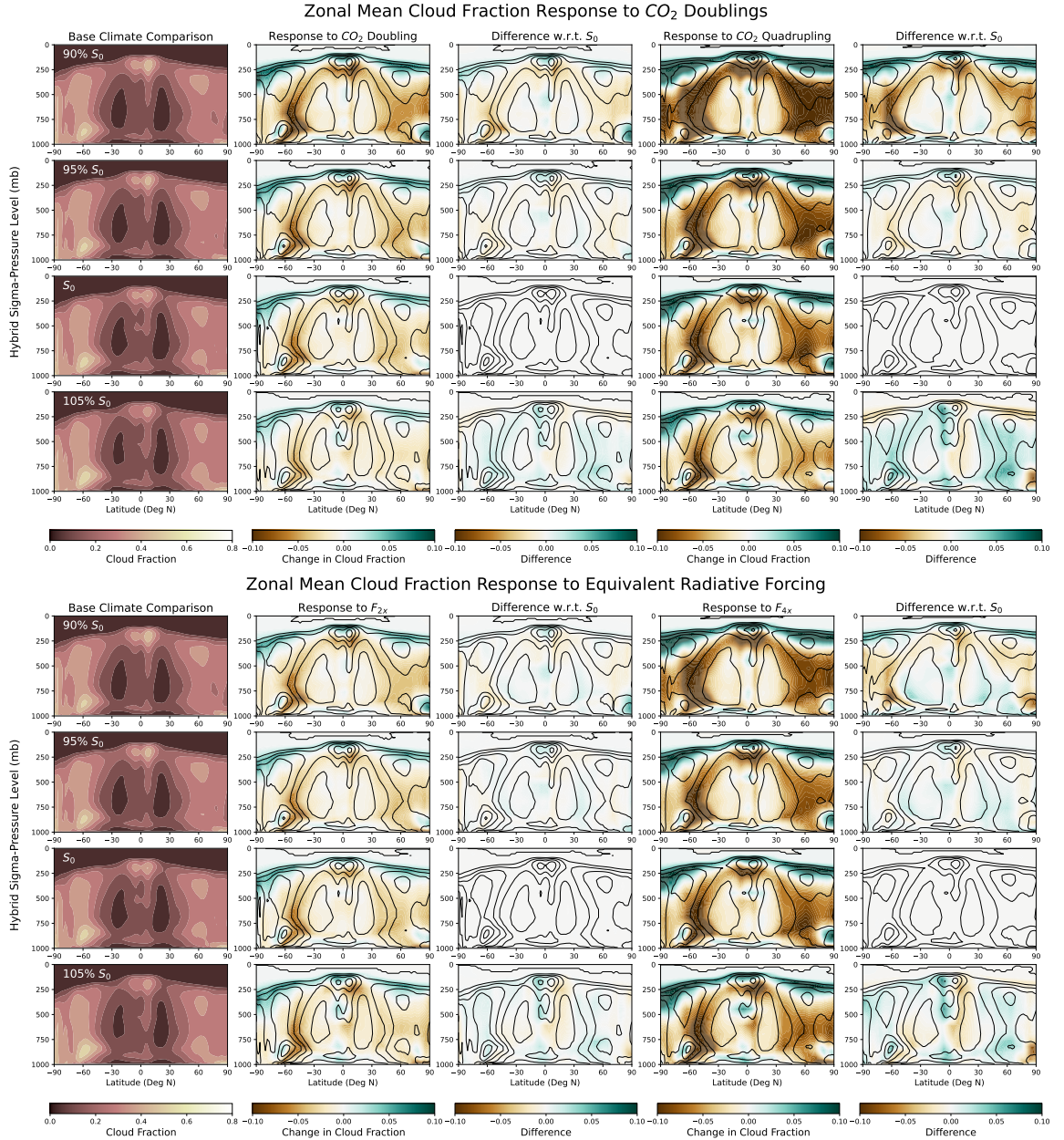


Figure 3.9: Zonal Mean Cloud Fraction Response to CO₂ Increase. Control simulation is shown in the lefthand column, while doubling responses and the difference in response from the modern case are shown from left to right. For the difference fields, black contours depict the field's raw value, while colors represent the differences with respect to the present day case. Most prominent changes are the elevation of high-altitude clouds, and reduction of low level clouds in mid latitudes.

on changes in circulation. We measure baroclinicity of the atmosphere using eddy kinetic energy (Equation 2.3). Eddy kinetic energy is found to decrease in magnitude within the bulk of the mid-latitude storm track. Additionally, an increase in EKE can be seen poleward of the southern hemisphere EKE minimum, and this is consistent with the accepted idea in literature that mid latitude storm tracks shift poleward with increased CO₂ concentrations [Hall et al., 1994] [Bender et al., 2012] [Mbengue and Schneider, 2013]. Reductions in EKE (Figure 3.12) are found at the same latitudes as decreases in low cloud fraction (Figure 3.9 and 3.10). This correlation is quantified in

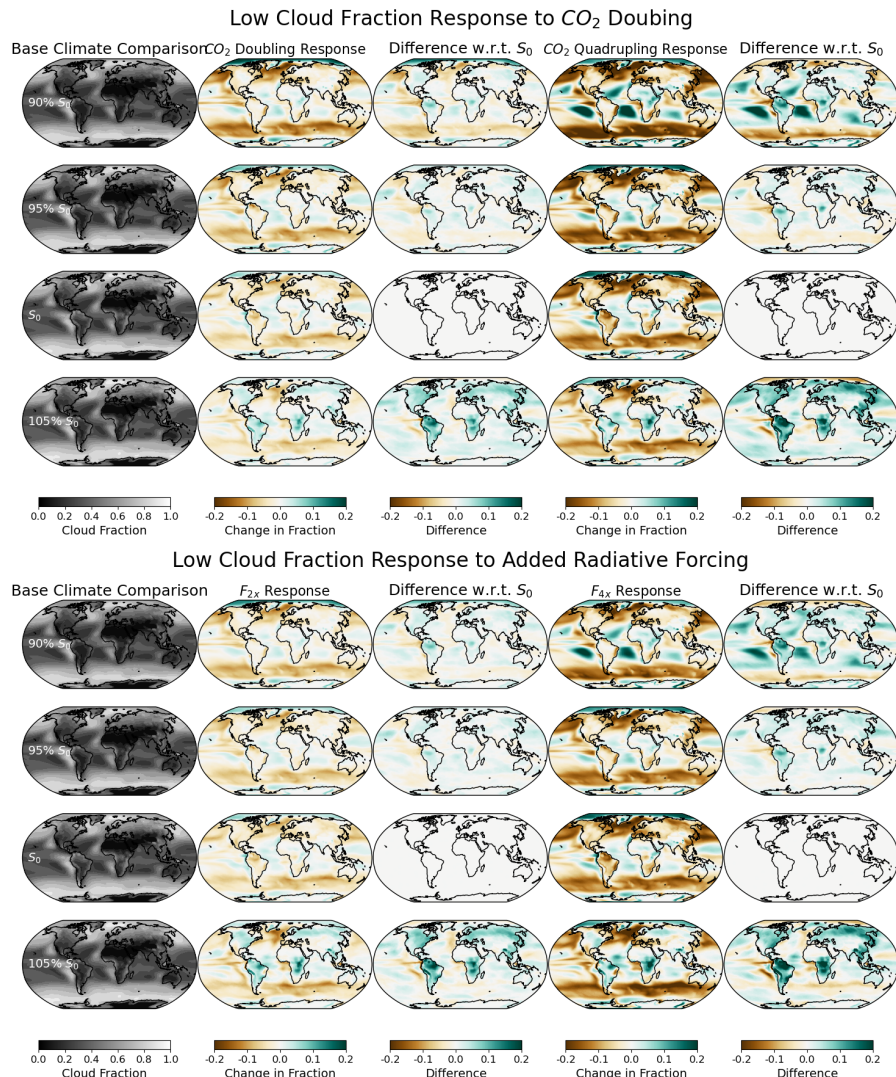


Figure 3.10: Low cloud fraction response to CO₂ increases for each simulated climate state. Control simulation is shown in the lefthand column, while doubling responses and the difference in response from the modern case are shown from left to right.

Figure 3.13 using a linear regression on each gridbox data point of low cloud fraction response and EKE response. This supports the idea that weaker baroclinic eddies are related to the observed reduction in low cloud fractions.

In contrast to the mid latitude response, the poles experience a pronounced increase in low cloud fraction with CO₂ increase. The increases in low cloud fraction here are tied to the exposure of the arctic ocean after sea-ice melt due to warming. The melting of sea ice allows for greater sea-to-air moisture flux through surface evaporation and wave-driven sea spray [Kay and Gettelman, 2009]. Figures 3.15 and 3.16 supports this notion, comparing the reductions in sea ice associated with

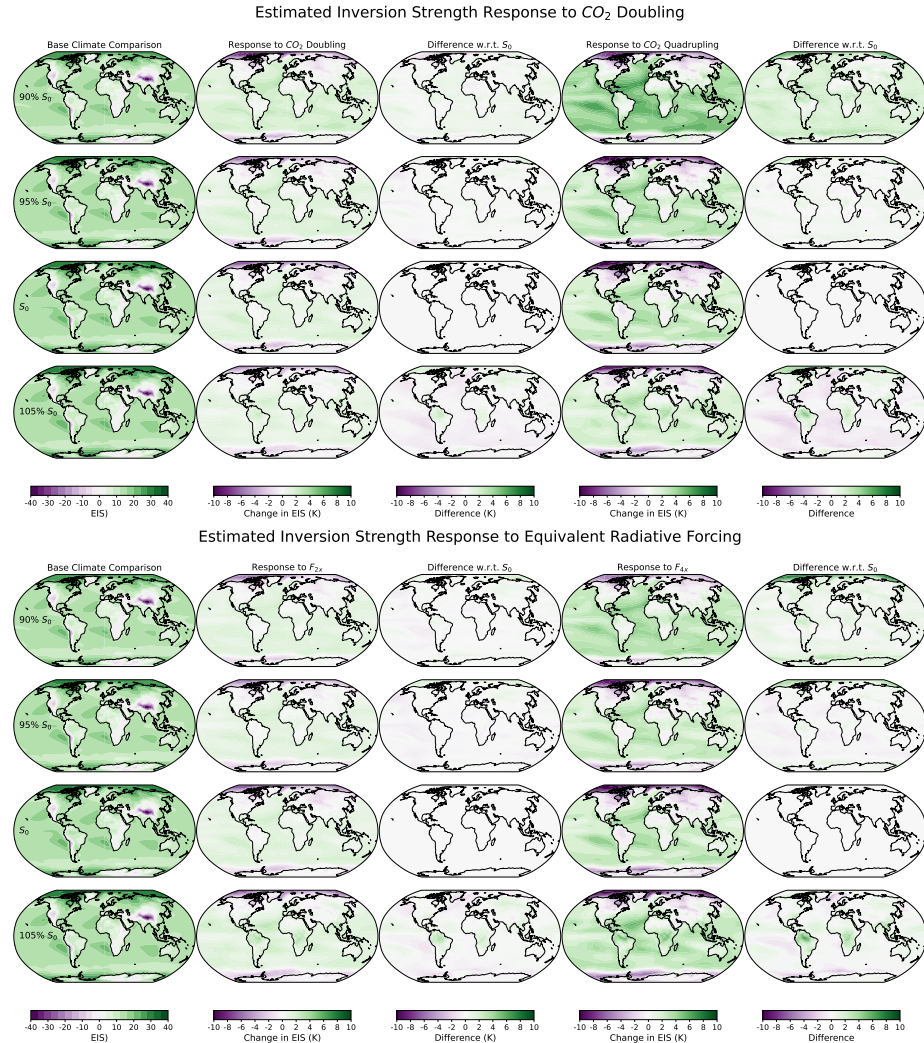


Figure 3.11: Change in estimated cloud top inversion strength in response to added CO₂. Control simulation is shown in the lefthand column, while doubling responses and the difference in response from the modern case are shown from left to right.

CO_2 doubling and quadrupling to increases in low cloud fraction. The strong spatial correlation seen between low cloud fraction increases and loss of sea ice, as well as the similar dependence on background climate state, is enough to conclude that increases in low cloud fraction are due to additional moisture flux from an exposed polar ocean[Bintanja and Seltjen, 2014][Singh et al., 2017]. Similar effects can be seen in Figure 3.16, however not as pronounced due to the presence of the Antarctic continent. In addition, it is unclear whether the increases in low cloud fraction observed

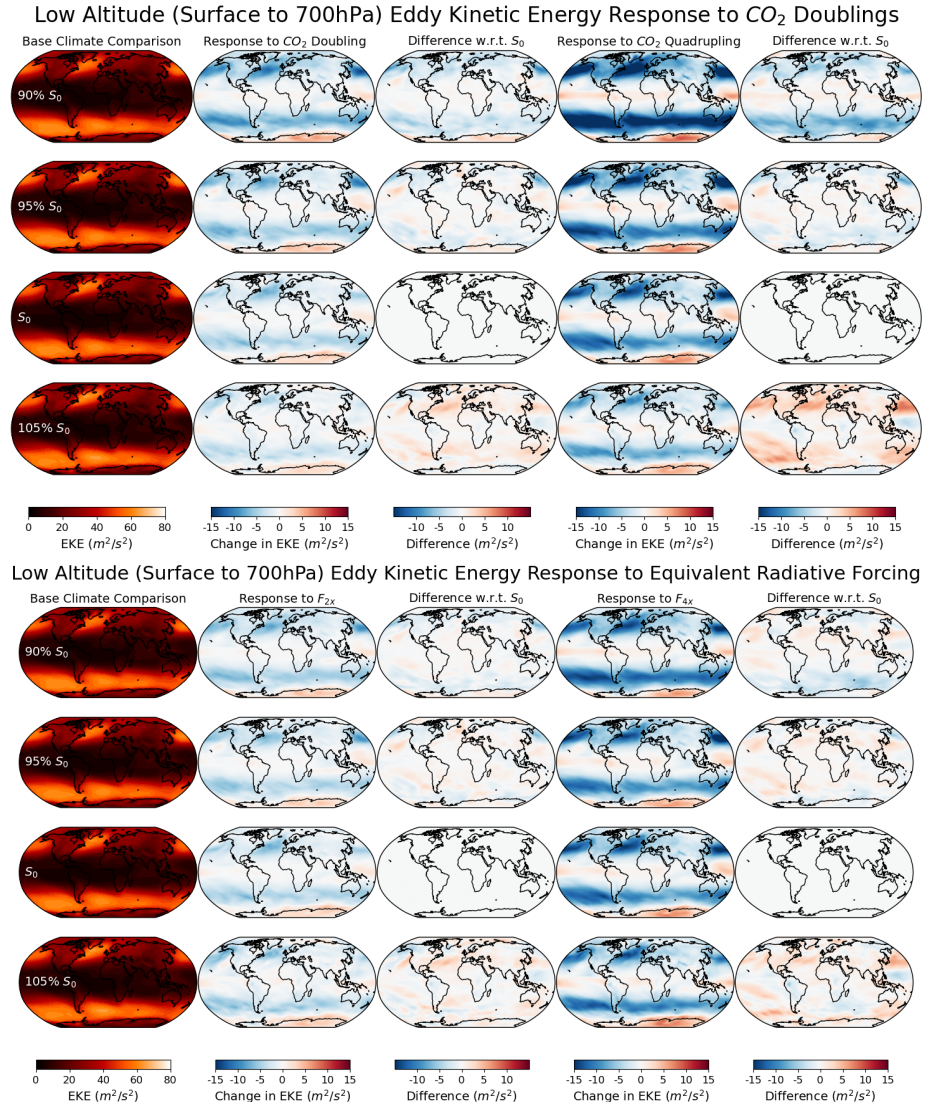


Figure 3.12: Eddy Kinetic Energy Response to Added CO_2 . Control simulation is shown in the lefthand column, while doubling responses and the difference in response from the modern case are shown from left to right.

Low Cloud Fraction Response and Low-Level Eddy Kinetic Energy Response Regression

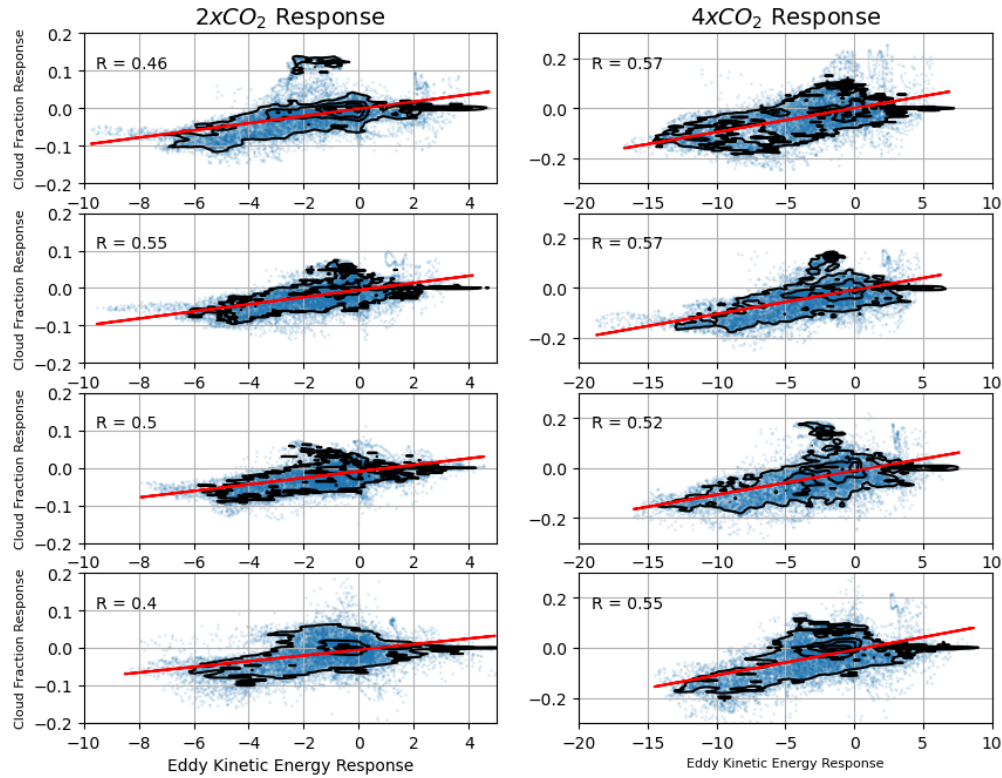


Figure 3.13: Linear Regression between low cloud fraction and eddy kinetic energy CO₂ doubling (left) and quadrupling (right) responses. each data point represents a value at a single latitude-longitude gridbox

are due to reductions in sea ice entirely, or in part due to the poleward shift in mid latitude storm track..

An important detail is the impact that more low clouds have on the local energy budget in the polar regions. The shortwave cloud radiative response in the arctic still dominates the longwave cloud radiative response; however, these new clouds form in wake of the loss of sea ice, which is already very reflective. This change is seen in all seasons, with the strongest response occurring in the Northern hemisphere Summer. For seasons that provide the poles with shortwave energy, the increase in shortwave cloud forcing here is dwarfed in comparison with the decrease in up-welling TOA shortwave flux had from sea ice loss, and therefore the longwave cloud radiative effect now dominates the change in the regional radiation budget that clouds impose. The same can be said for polar winters, where clouds have no shortwave radiative effect to begin with. Seasonality of sea ice and low clouds in the Arctic is represented in

Figure 3.14.

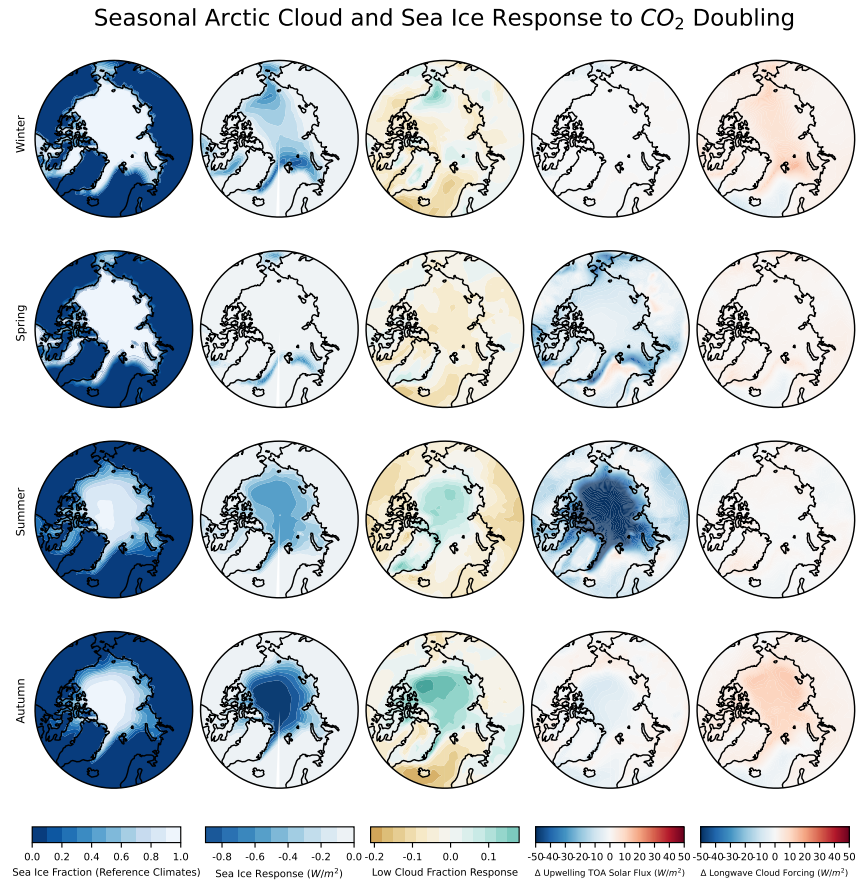


Figure 3.14: Arctic sea ice and low cloud fraction response to added CO_2 in each season for the control run with pre-industrial conditions. Seasons are in descending order of Winter, Spring, Summer, and Autumn. The lefthand column depicts sea ice fraction before CO_2 doubling, and every other column depicts responses to CO_2 doubling.

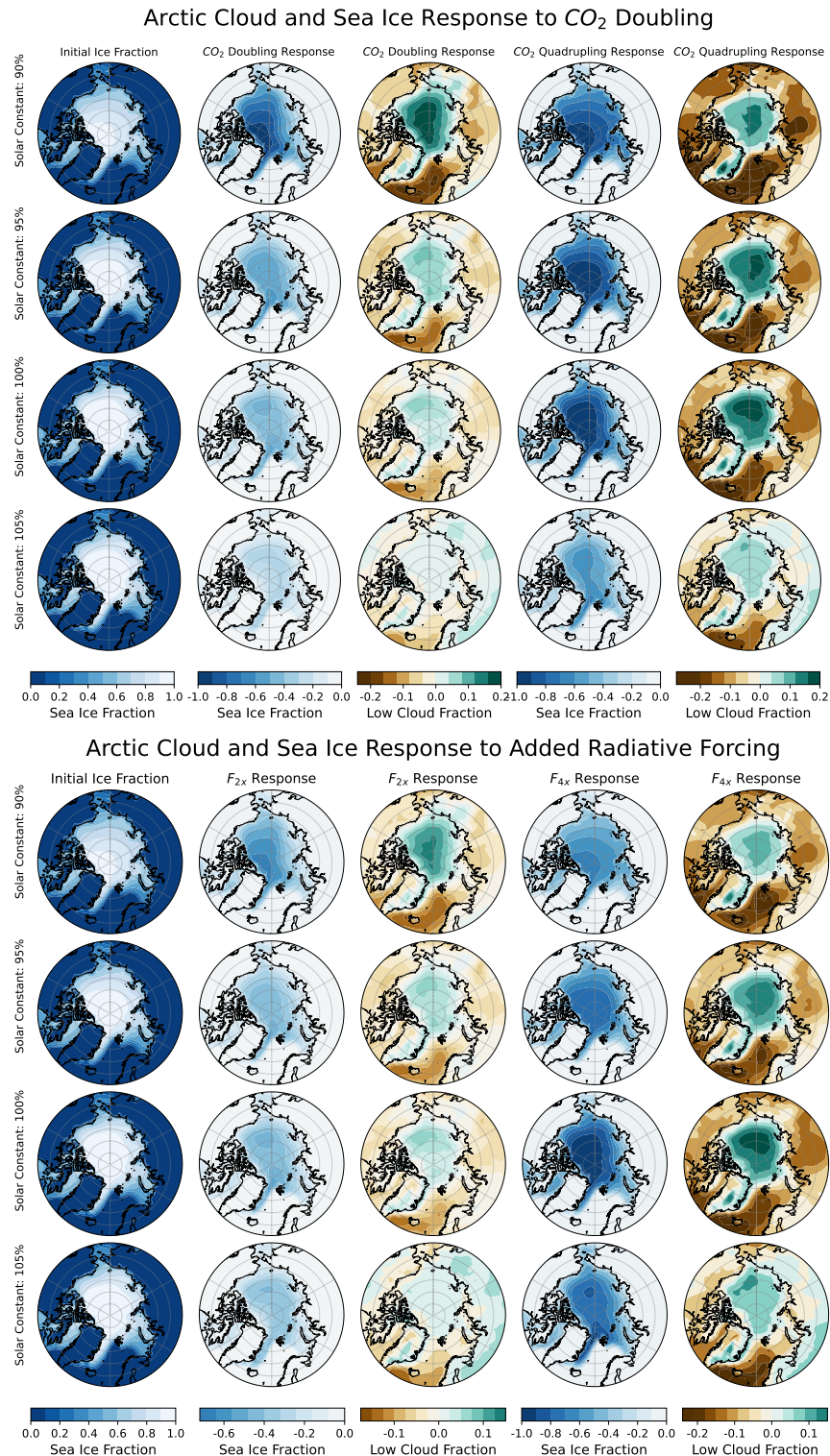


Figure 3.15: Arctic sea ice and low cloud fraction response to added CO_2 . Control simulation is shown in the lefthand column, while doubling responses and the difference in response from the modern case are shown from left to right.

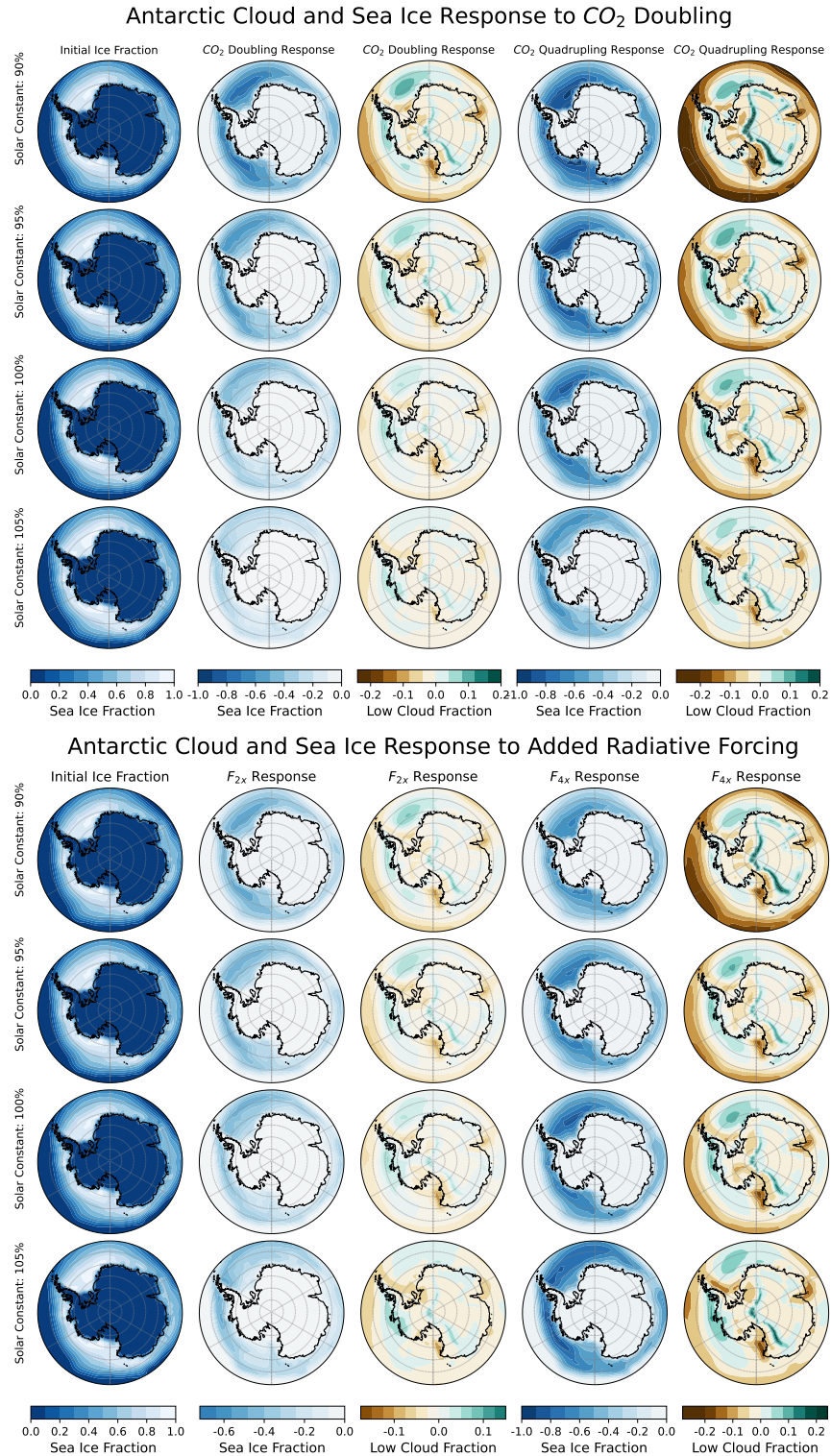


Figure 3.16: Antarctic sea ice and low cloud fraction response to added CO_2 . Control simulation is shown in the lefthand column, while doubling responses and the difference in response from the modern case are shown from left to right.

In general, the loss of low clouds seen in the mid latitudes due to a reduction in atmospheric baroclinicity dominates the overall response of clouds to added CO_2 radiative forcing. While we do observe an increase in low clouds over the polar regions, their concurrence with sea ice loss subtracts from the net change in albedo and the effect they have on the global energy budget. The impacts that these responses have on the global shortwave cloud forcing distribution can be seen in Figure 3.17. Increases in cloud forcing (meaning reductions in reflective clouds) occur most strongly over mid latitudes, while decreases in cloud forcing occur over the arctic and antarctic. The loss of shortwave cloud forcing with warming leads to a positive cloud feedback in temperature, where less low cloud results in increased warming.

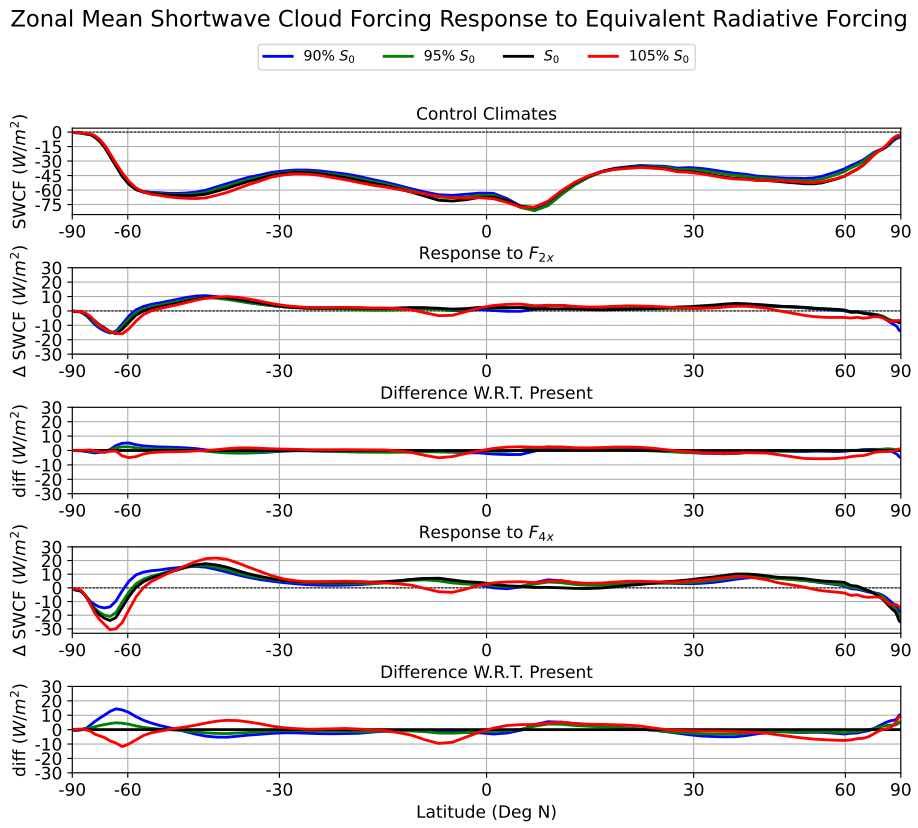


Figure 3.17: Zonal Mean shortwave cloud forcing response to present-equivalent CO_2 radiative forcing. base climate state values are shown in the top panel, while 2x and 4x radiative forcing responses and their differences with respect to present day responses are shown from the top down. Each line represents values for a given solar case S/S_0 .

3.5 High Clouds

High cloud responses to CO₂ are mostly consistent for each climate state. The most prominent change seen is a vertical elevation of the high cloud deck across all latitudes, seen in Figure 3.9 as an increase in cloud fraction above the climatological high cloud deck and a decrease beneath it. This is a well understood side effect of tropospheric warming, as the atmosphere expands and pushes the tropopause to higher altitudes, known as the cloud altitude feedback [Manabe and Wetherald, 1975][Ceppi et al., 2017].

There are stark differences between the late-analog climate response and the rest of the simulated climates (Figure 3.18). The late-analog climate response depicts stronger increases in high cloud fraction, particularly in the southern hemisphere. These increases in high cloud fraction are well aligned with the observed southward shift in the ITCZ, and this can also be seen in Figure 3.20 as a southward shift in tropical longwave cloud forcing.

A proposed reason for this is the presence of anomalously high sea surface temperatures in the Southern Hemisphere, which are more conducive to deep convection and therefore generate more high clouds in the tropics. Both increases in high cloud fraction and higher sea surface temperatures are indeed observed in this region of the equatorial east Pacific ocean in Figure 3.19.

Other high cloud changes are reflective of changes in the global mean circulation. As mentioned earlier, in all cases we observe a systematic reduction in the strength of the Hadley circulation. This is important in the context of high clouds because a majority of high cloud moisture is sourced from tropical convection, and advected to higher latitudes. As a consequence of the deep tropical squeeze effect [Lau and Kim, 2015], high clouds are more prevalent immediately at the equator, but are less prevalent in the shallow tropics and subtropics. This can be seen as a double-trough pattern in the tropical belts of Figure 3.20

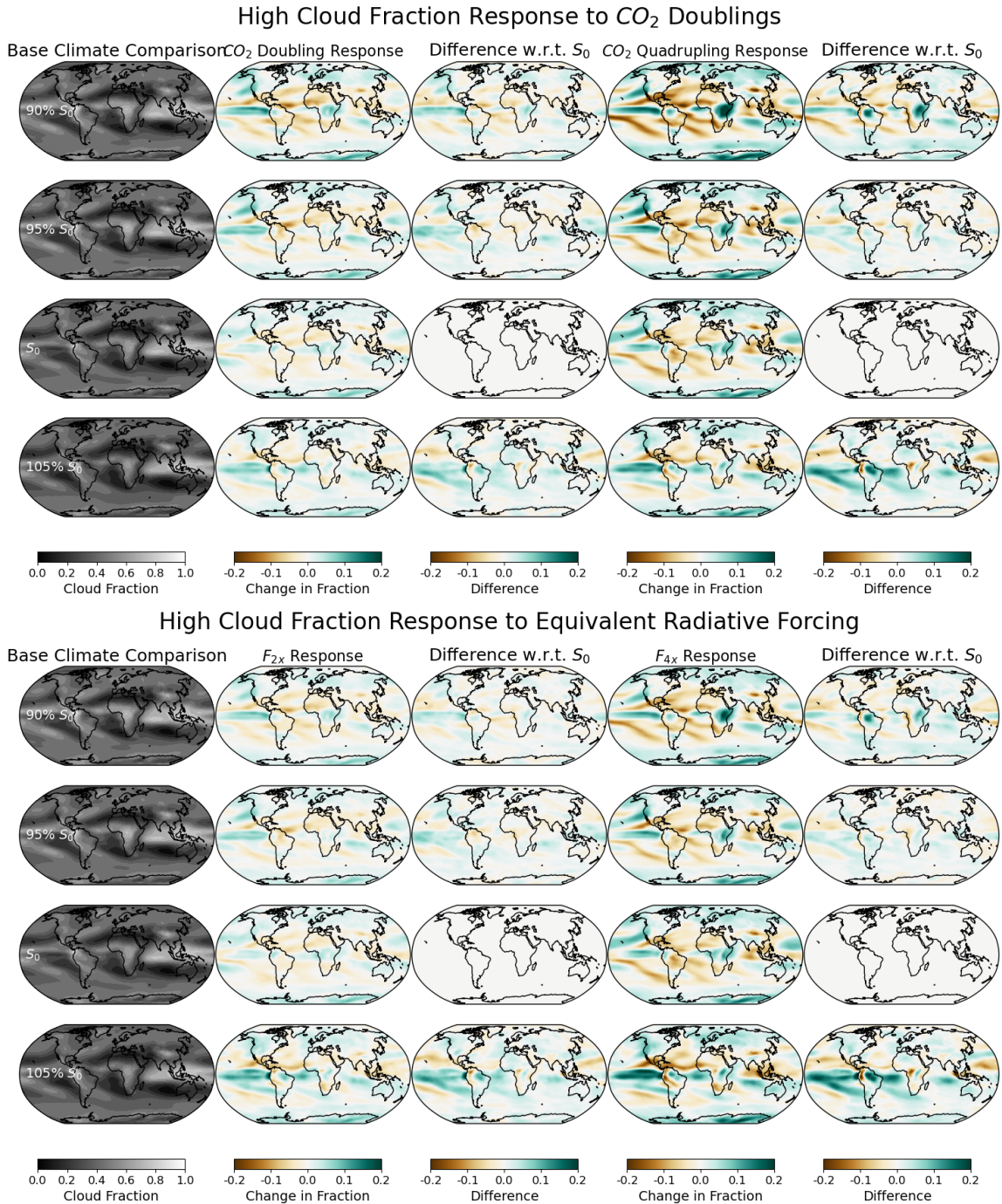


Figure 3.18: High Cloud Fraction Response to added CO₂. Control simulation is shown in the lefthand column, while doubling responses and the difference in response from the modern case are shown from left to right.

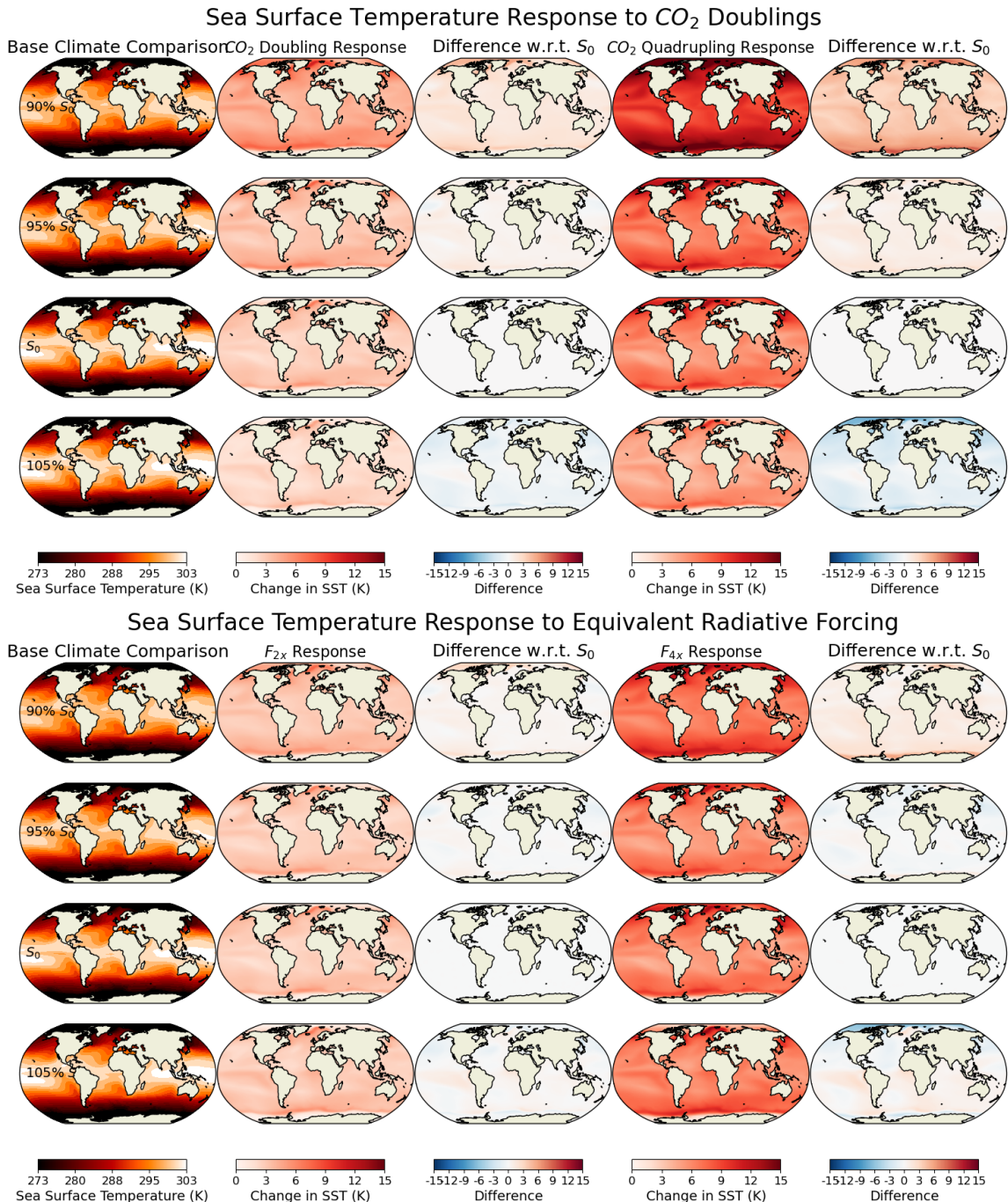


Figure 3.19: Sea surface temperature response to added CO_2 . Note the anomalously warm waters present in the Southern Hemisphere of late-analog climates, most readily seen in difference panels. Control simulation is shown in the lefthand column, while doubling responses and the difference in response from the modern case are shown from left to right.

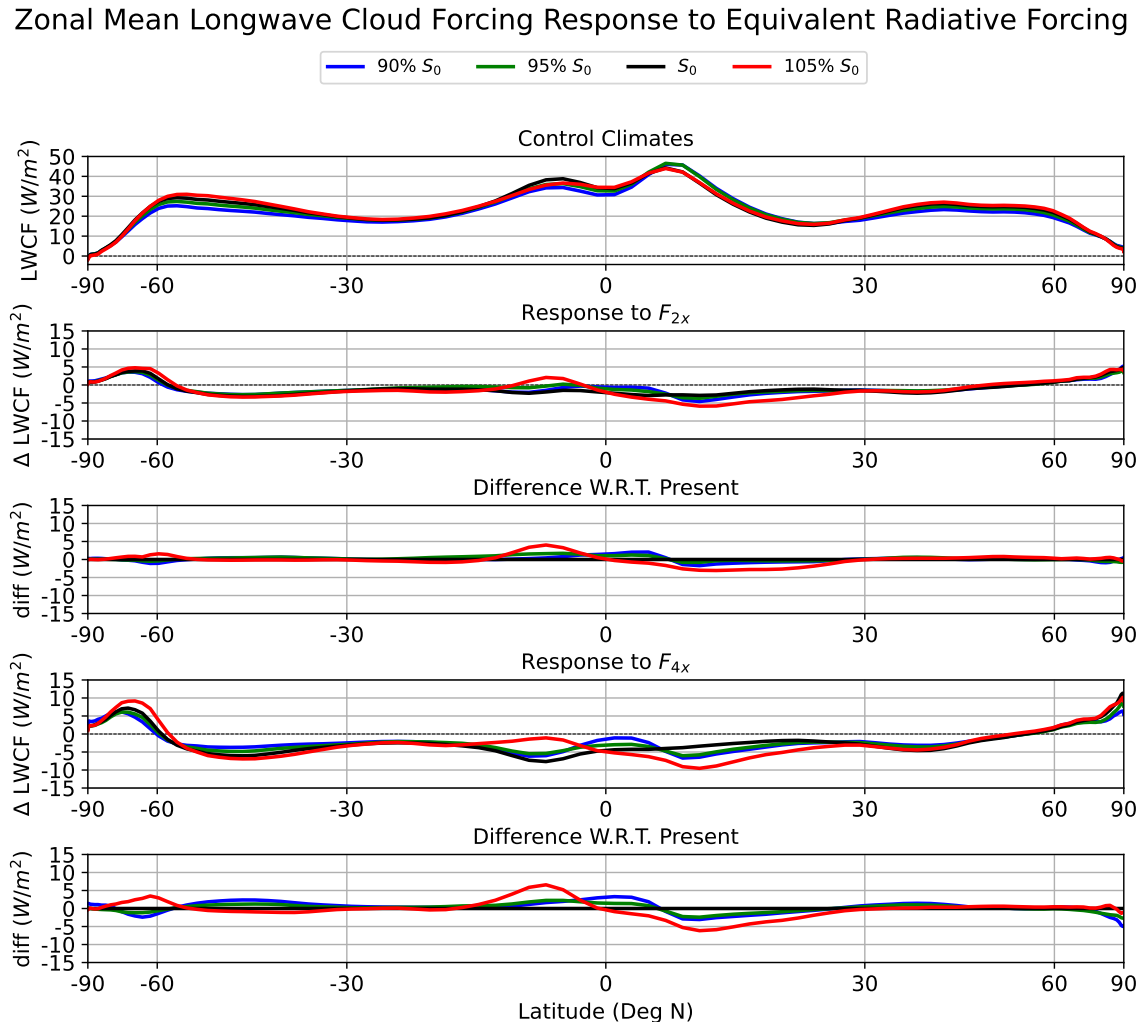


Figure 3.20: Zonal mean longwave cloud forcing response to present-equivalent CO_2 radiative forcing. Control simulation is shown in the top row, while 2x and 4x radiative forcing responses and their differences are shown from the top down. individual lines represent values for a given solar case S/S_0

3.6 Cloud Microphysics

When considering cloud radiative feed backs to CO₂ increases, micro-physical changes are just as important as synoptic and regional changes. As elucidated in the Introduction, the radiative properties of clouds depend heavily on the size and state of the particles that comprise them. We first observe phase changes of cloud particles (Figure 3.20). Consistently, cloud water transitions from ice to liquid phase in response to CO₂ doubling. This is an expected result, since cloud ice particles should more frequently melt and therefore be less common under warmer conditions. While the response of cloud liquid water is consistent with the magnitude of radiative forcing, the response of cloud ice water is not so. More rigorous convection over equatorial rain-forests for the early-analog 4xCO₂ climate state provides additional cloud ice water through increased cirrus fraction, which may explain the inconsistent response of cloud ice for this climate regime (Figure 3.18). The effect that the transition from ice to liquid has on the climate is still an active area of research [Gettelman and Sherwood, 2016][Ceppi et al., 2017], however liquid droplets for clouds tend to be more reflective of solar radiation than ice crystals [Stephens et al., 1990][Sun and Shine, 1994]. We can infer that the transition from ice to liquid within clouds would result in a negative shortwave cloud radiative feedback.

In addition, we also observe changes in cloud droplet radii. The albedo of a cloud with more, smaller cloud droplets will be greater than for a cloud with fewer and larger droplets, for a given cloud water content [Brenguier et al., 2000]. We analyze the change to inferred cloud droplet radii for each of our climate states, seen in Figure 3.21. There are systemic increases in cloud droplet radius for each simulated climate state, increasing by about 5% per CO₂ doubling. These increases are remarkably consistent for each climate state. This increase is reached through a decrease in cloud droplet number concentration, along with an increase in total cloud liquid water in the atmosphere. The increase in cloud liquid comes from the transition from cloud ice to cloud liquid and an increase in evaporation with warming, and therefore condensation in clouds, assuming a hydrological cycle in equilibrium [Betts and Harshvardhan, 1987]. The decrease in cloud droplet number concentration can be attributed to an increase in liquid droplet deposition, as larger droplets tend to precipitate out more frequently as drizzle [Albrecht, 1989]. We only consider cloud liquid water for calculation of inferred droplet radius because of the complex statistical distribution of shapes of ice particles, which is beyond the depth of this study.

Global Mean Cloud Phase comparison and response to Added Radiative Forcing

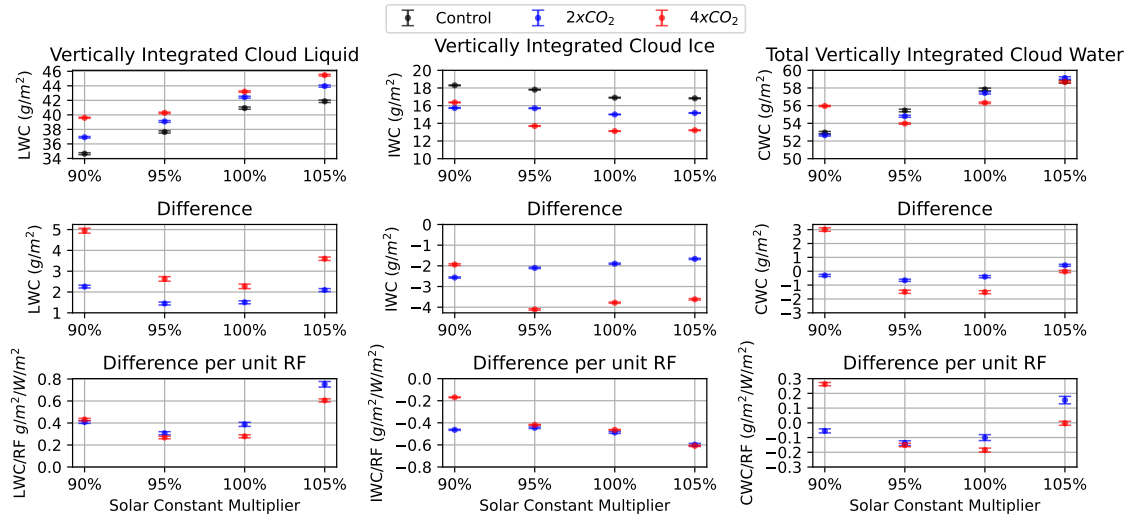


Figure 3.21: Global mean cloud liquid water path (right), cloud ice water path (center), and total cloud water path (right) for each simulated climate state (top), responses to CO₂ doubling (middle), and responses per unit radiative forcing for each case (bottom). Error bars are calculated using standard error across all monthly model output.

It is important to understand that the reduction in column cloud droplet number is affected by changes to cloud fractional occurrence. We might assume that the reduction in column droplet number globally is indicative of less cloud condensation nuclei (CCN) in the atmosphere. Instead, we find that CCN concentrations tend to increase with warming (Figure 3.22). This demonstrates that large scale changes to the climate at the global and regional level have impacts on the micro-physical properties of clouds such as droplet radius, and transitively, cloud optical depth.

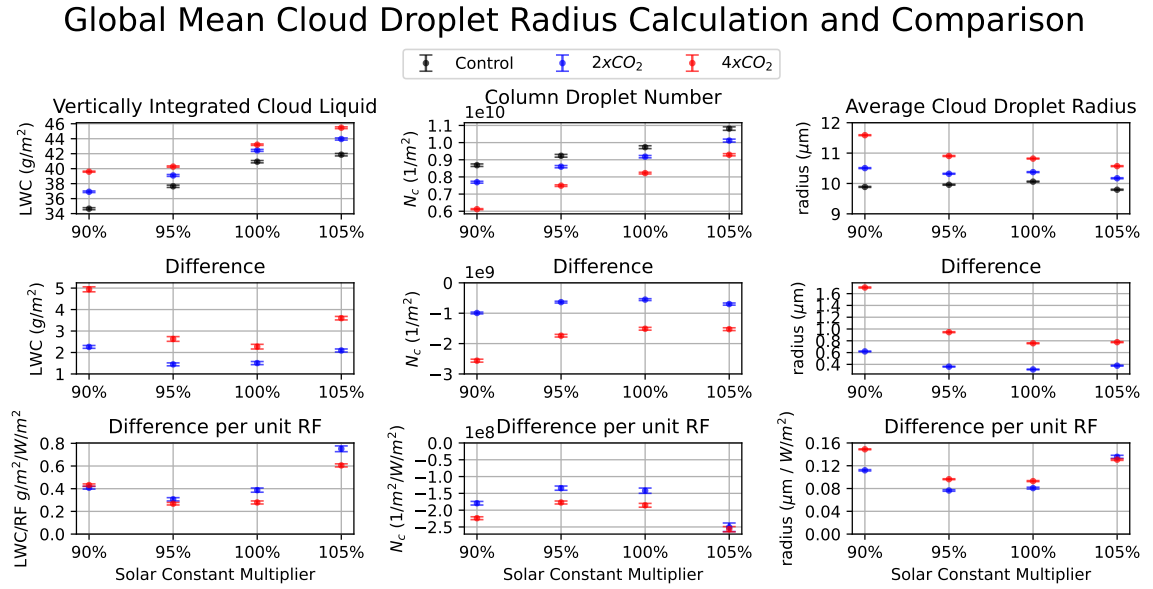


Figure 3.22: Global mean cloud liquid water path (right), cloud droplet column number (center), and inferred cloud droplet radius (right) for each simulated climate state (top), responses to CO_2 doubling (middle), and responses per unit radiative forcing for each case (bottom). Error bars are calculated using standard error across all monthly model output.

3.7 Global Mean Response of Clouds

The overall response of clouds to increased radiative forcing from CO_2 is very consistent across each climate state. Figure 3.24 shows the global mean shortwave, longwave and net cloud radiative responses to doubling CO_2 . In each experiment, The shortwave cloud radiative effect decreases in magnitude due to a reduction in reflective clouds, leading to an additional $0.4\text{--}0.5 W/m^2$ of cloud radiative feedback per unit of CO_2 radiative forcing. This decrease can be attributed to systematic reductions in optically thick low clouds (Figure 3.10). The longwave cloud radiative effect also decreases in magnitude, by about -0.2 to $-0.3 W/m^2$ of cloud radiative feedback per W/m^2 of CO_2 radiative forcing. With the exception of the late-analog climate state, because the shortwave cloud radiative response to CO_2 doubling is stronger than the longwave cloud radiative response, we observe an additional 0.15 to $0.2 W/m^2$ of net cloud radiative feedback per W/m^2 of CO_2 radiative forcing.

Figure 3.25 shows what latitude regions influence the global shortwave cloud radiative effect the most. The relative contributions of each latitude band are parts of the whole global mean cloud radiative effect. For example, the sum of each band's

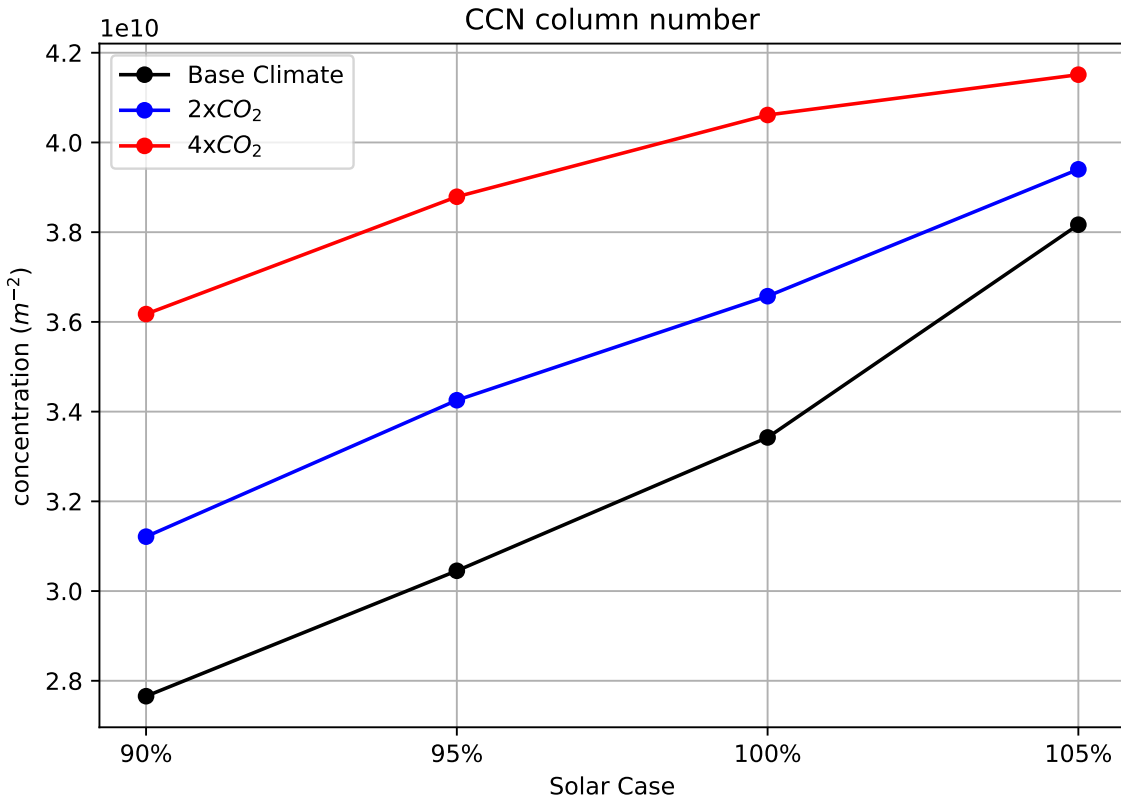


Figure 3.23: Global mean cloud condensation nuclei column number for background climate states (black), CO_2 -doubled (blue) and CO_2 -quadrupled (red) climate states.

cloud radiative effect equals the global mean cloud radiative effect.

The most influential response to CO_2 doubling comes from the mid latitudes, where the observed reductions in cloudiness in the mid-latitude storm track are located, in spite of the fact that the Tropics maintain the most dominant influence on the global mean shortwave cloud radiative effect. As seen in Figure 3.17, the greatest responses in shortwave cloud forcing occur in the southern ocean, where the reduction in baroclinicity leads to weaker cloud coverage over the mid-latitude storm tracks. In the polar regions, increases in shortwave cloud forcing can be seen due to the previously stated reductions in sea ice; however, the effect of a weaker mid latitude storm track bleeds over into the high-latitude partition defined for regional contributions, explaining the high latitude partition's smaller total share of the global mean shortwave response. Effectively, this tells us that the changes to cloud forcing felt in the mid latitudes have the greatest impact on the total global response to CO_2 doubling.

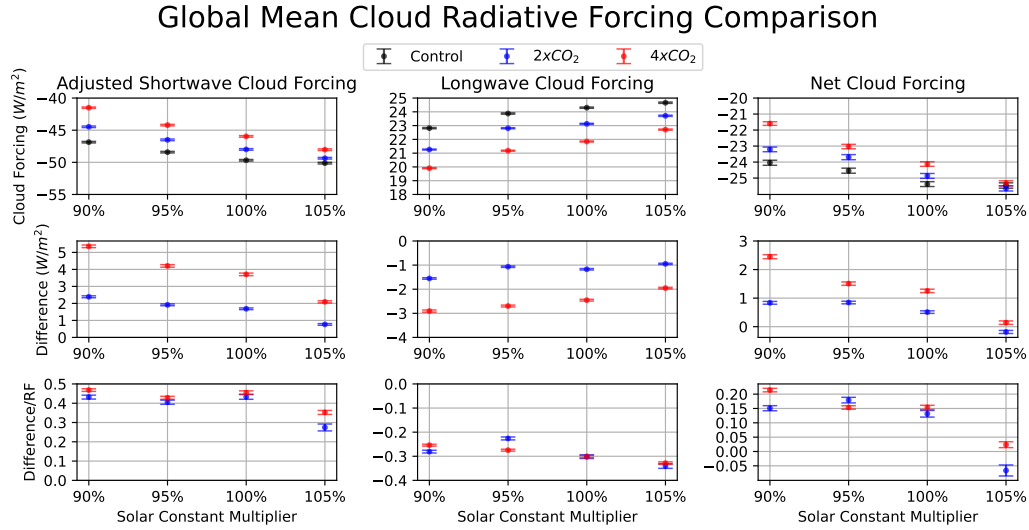


Figure 3.24: Global Mean shortwave (left), longwave (center), and net (right) cloud radiative effects (top), response to CO₂ doubling (middle), and response normalized to radiative forcing for each case (bottom). Error bars are calculated using standard error across all monthly model output.

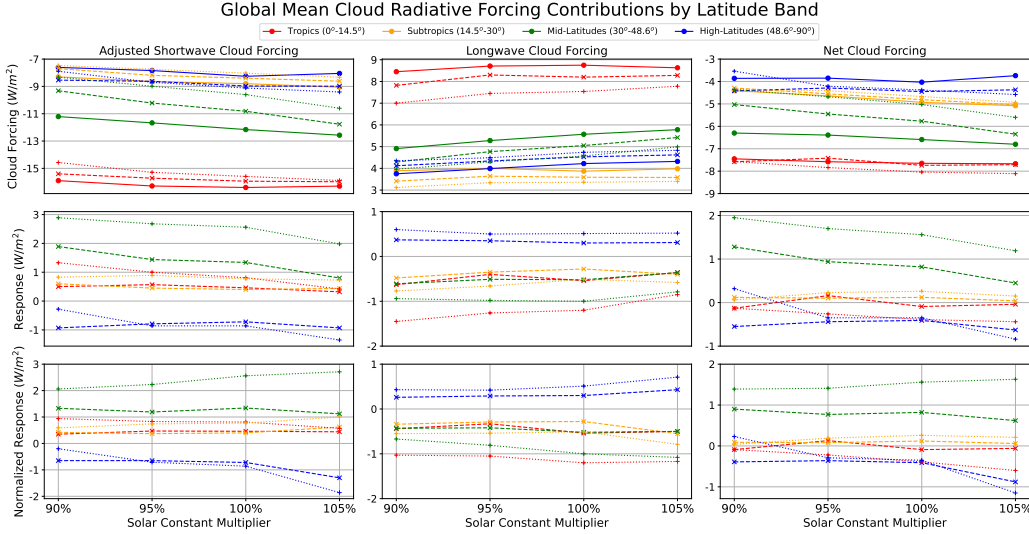


Figure 3.25: Relative Contributions by latitude band to global mean shortwave (left), longwave (center) and net (right) cloud forcing response to CO₂ doubling. The sum of each band contribution for each climate state is equal to the global mean cloud forcing for that climate state. Each band has the same surface area and represent the tropics, subtropics, mid-latitudes, and high latitudes in ascending order of latitude. Control climates are depicted by a solid line, CO₂ doubled climates by a dashed line, and CO₂ quadrupled climates by a dotted line.

Though the response of shortwave cloud forcing in lower latitudes is still significant compared to the larger response in the mid latitudes, the opposite is true for the longwave cloud forcing response. The deep tropical squeeze effect conceived by Lau and Kim [2015] results in an increase in high cloud fraction in the deep tropics, but a decrease in high cloud fraction in the shallow tropics and subtropics. This actually results in a net decrease in the overall longwave cloud radiative effect for these partitions, because changes in high cloud fraction are more important in the shallow tropics and subtropics, where net subsidence regions are drier and permit more infrared radiation to escape to space than in humid equatorial regions. This effect is most strongly seen in the northern hemisphere in Figure 3.20. Though a decrease in longwave cloud forcing is felt globally in all regions, it is most strongly felt in these drier shallow tropical regions.

The consequence to this is that the response of the net cloud radiative effect is small for low latitudes and high latitudes, but significant for the mid-latitudes (Figure 3.26). Additionally, the overall response of cloud forcing for each latitude region is consistent for early-analog climates and the present day climate state.

The late analog CO₂ doubling case is the only exception to this, where the tropical response is larger than the mid-latitude response. A potential reason we may observe this inconsistency is the prevalence of anomalously high sea surface temperatures in the southern hemisphere, which could promote persistent convective weather patterns as seen in the Amazon and African rain-forest biomes, seen in cloud fraction responses to CO₂ doubling (Figures 3.18). The presence of persistent optically thick deep convective clouds in these locations would result in a perceptible decrease in shortwave cloud forcing (increase in reflective clouds), which is what we observe. Nevertheless, we conclude that the mid latitudes are most responsible for the change in cloud radiative forcing, and that these responses in cloud forcing are consistent for each climate state.

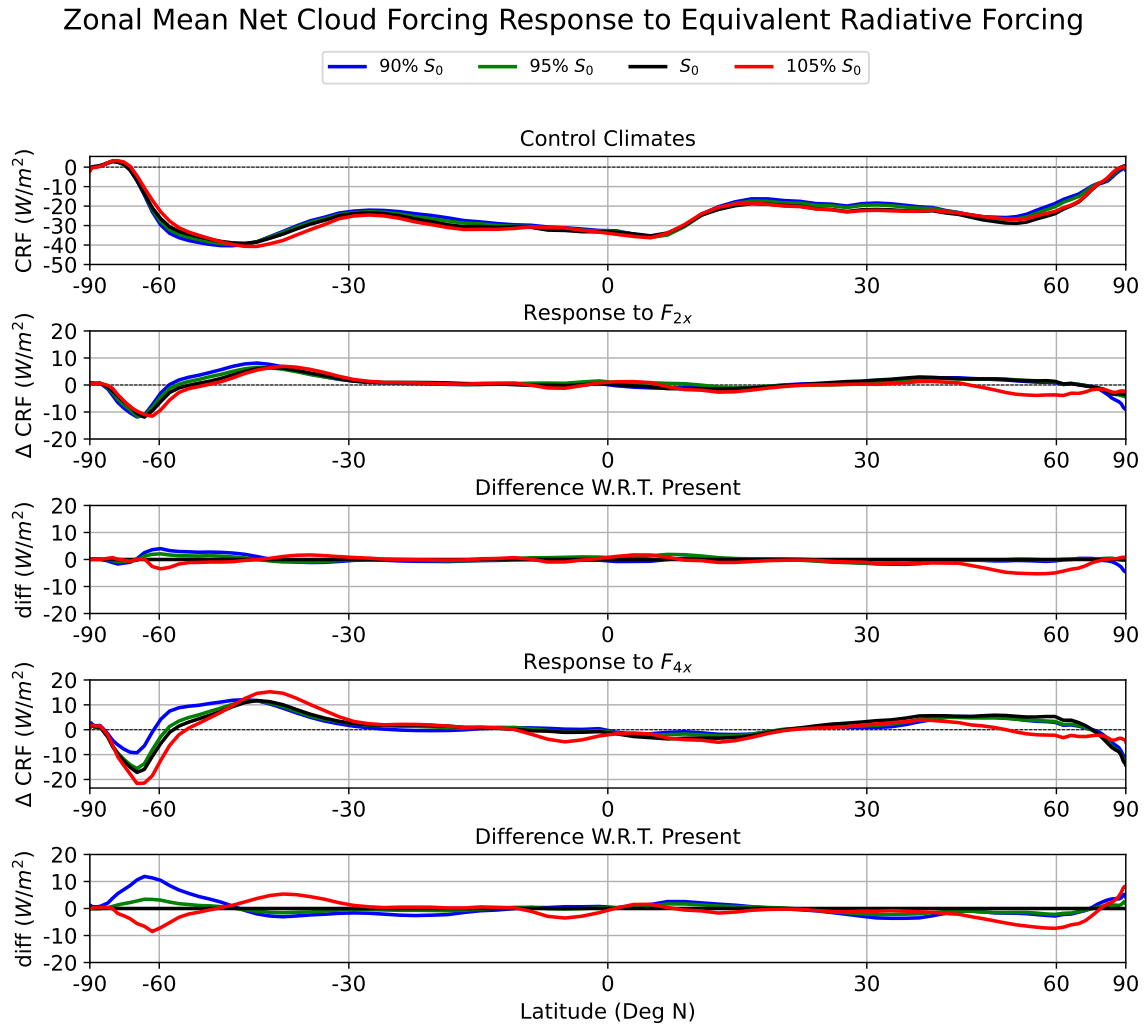


Figure 3.26: Zonal mean net cloud forcing response to present-equivalent CO_2 radiative forcing. Control simulation is shown in the top row, while 2x and 4x radiative forcing responses and their differences are shown from the top down. individual lines represent values for a given solar case S/S_0

Chapter 4

Discussion

4.1 Conclusion

The results of this study determine that the most influential changes to clouds in response to an increase in CO₂ radiative forcing are consistent for each climate state. Differences in the response of clouds and circulation do not appear to inflict substantial change to the global cloud radiative effect. The change in clouds most influential to the shortwave cloud radiative effect is the loss in low cloud fraction observed in the mid-latitude storm track, where reduced baroclinic activity in the presence of a more shallow EPTG results in less cloud formation through synoptic ascent. Changes to clouds most influential to the longwave cloud radiative effect are reduction in high cloud fraction that occurs in the subtropics and mid-latitudes. Polar clouds change in contrast to the global mean response, providing an increase in shortwave cloud forcing through increased occurrence of low level marine stratocumulus, though we deem these changes as less influential toward the net global cloud forcing response due to their conflict with the radiative effect of sea ice loss from which these clouds form during seasons with incident shortwave radiation, and the lack of importance of sea ice in winter seasons.

The results of this study also determine that specific climate sensitivity is independent of differences in background climate state. Past studies such as Caballero and Huber [2013] and Hansen et al. [2013] determine that the primary reason for differences in specific climate sensitivity in their experiments stems from cloud radiative feedbacks in response to each consecutive CO₂ doubling. Specific climate sensitivity shown in our study remains approximately constant for each CO₂ doubling. This

finding compliments the results of these studies: if specific climate sensitivity depends on differences in cloud feedbacks between climate states, then the consistent response of clouds to CO₂ doublings found in this study should and does render invariant climate sensitivities. These past studies evaluate state dependence at different temperatures. In this study, climate sensitivity and cloud forcing responses to CO₂ doublings are found to be consistent for climates with near-equal GMST, achieved by varying both CO₂ concentration and incident solar insolation. In addition to verifying the dependence of specific climate sensitivity on cloud feedbacks, this study concludes that said feedbacks and climate sensitivities are independent of differences between climate regimes where these two factors vary, provided each regime receives the same initial radiative forcing.

For early-analog climate states and the pre-industrial climate state, responses to CO₂ doubling per unit radiative forcing are relatively constant, but not so constant for some results in the late-analog climate state (including but not limited to: global mean vertically-integrated cloud liquid (Figure 3.20,3.21), circulation response (Figure 3.6,3.7)). A potential reason for this discrepancy is the presence of higher sea surface temperatures in the southern hemisphere, resulting in increased occurrence of low and high clouds. It is not clear what the cause of these anomalously high SST values are. Natural variability is obviously responsible to some degree here, but the actual mechanism behind the higher temperatures are unknown. Persistent El-Nino-like conditions are present as well, and one may be tempted to blame this teleconnection for the SST pattern observed; however, these simulations use a slab ocean, and the ocean dynamics necessary to develop the El Nino Southern Oscillation do not exist. A large fraction of models used in the Coupled Model Inter-comparison Project (CMIP3 & CMIP5) exhibit multi-decadal El-nino-like conditions [Collins et al., 2010][Huang and Ying, 2015][Ying et al., 2016][Zheng et al., 2016], owing to the weakening of the Walker circulation in response to warming from added CO₂ by Held and Soden [2006] and Vecchi and Soden [2007], so this may also be responsible for the observed SST pattern, though we might also expect to see this in the other climate configurations as well. Some responses to CO₂ increases such as those in Figures 3.6, 3.10, and 3.18, are different in similar fashion for solar cases apart from the present-day analog climate, despite their oppositional differences in solar insolation and background CO₂ concentration. It is unclear what the cause of this discrepancy is; initially it was thought that errors in constrained GMST for initial climate states may have affected results that are temperature sensitive in a similar manner (e.g. cloud fractional occurrence),

however given that the magnitude of the difference in GMST between each initial climate state is smaller than 0.1K and therefore not of great importance, this likely isn't the culprit behind this observed pattern.

4.2 Caveats and Shortcomings

This study comes with several caveats that should not be ignored. Firstly, this study assumes that the use of the CESM is practical in a paleoclimate context; however this model was constructed initially for studies involving Earth's modern climate. Pushing certain configurations of the model away from modern conditions, such as reducing solar insolation or increasing CO₂, could therefore produce spurious results [Goldblatt and Zahnle, 2011]. We accept this in spite of this risk, as use of a state-of-the-art GCM allows us to analyze cloud feedbacks that would not be observable in a 1-dimensional radiative convective model.

Additionally, the model used in this study is one of many state of the art GCMs, coming out of the box with its own specific parameterizations for radiative transfer, cloud microphysics, and cloud dynamics. The use of any other climate model may impact the results to some degree. For example: CESM makes estimations of cloud condensation nuclei as a function of aerosol chemistry, temperature and vertical velocity, using the Kohler theory, as outlined in Abdul-Razzak and Ghan [2000]. Any model that estimates CCN concentration differently will have different running calculations for cloud droplet activation, which would consequently alter cloud radiative effect. In a more general scope, the Intergovernmental Panel on Climate Change 5th assessment report (IPCC AR5) [Flato et al., 2014] figure 9.7 compares the relative performance of each climate model contained in the Coupled Model Intercomparison Project 5 (CMIP5) using the root mean square error (RMSE) of key simulated variables. The difference in model performance (RMSE) arises from each model's individual parameterizations and defined physics schemes. CESM-CAM5, the model used in this study, has a slightly above average RMSE (worse) for longwave cloud radiative effect simulation, and a slightly below average RMSE (better) for shortwave cloud radiative effect simulation. It additionally scores a lower RMSE in other categorical variables such as upper and lower atmospheric temperature and wind speeds. For this reason, one can accept that the magnitude of the results may be slightly different if one were to use a different model for this experiment, but not so different that it would be detrimental to the validity of the results. It may be worth while to

grade different climate models individually based on the consistency of their climate sensitivities and cloud feedbacks in future work.

Finally, cloud responses to radiative forcing changes in this study are not officially “feedbacks” because they are not externally computed for a perturbation in radiative forcing after our simulations are ran. Proper calculation for “cloud radiative feedback” can be made using the partial radiative perturbation method [Wetherald and Manabe, 1988] or tools such as radiative kernels [Zelinka et al., 2012], however the course and depth of this study did not permit the use of such methods. The application of these techniques to quantify the magnitude of feedbacks described in this study is an attractive option to pursue for future work. Nevertheless, we accept these results as relevant in the pursuit of understanding cloud radiative feedbacks for different climate states.

4.3 Applications

These findings have important implications for paleoclimate studies. Past studies such as Caballero and Huber [2013] determine that climate sensitivity is dependent on background climate state due to positive cloud feedbacks. Here we demonstrate that significant differences in cloud responses to CO₂ doubling largely arise from differences in the magnitude of radiative forcing for each simulation’s CO₂ doubling alone. The idea that climate sensitivity and cloud radiative feedbacks are consistent with similar radiative forcings regardless of climatology simplifies the mission of understanding how cloud feedbacks influenced climates of the past.

This work is applicable to challenges in constraining Archean climate and resolving the faint young sun paradox. As mentioned prior, the early Earth was likely void of any glaciation, and the amount of CO₂ required to overcome the reduction in radiative forcing from a dimmer sun is inconsistent with geochemical proxy data [Rye et al., 1995] [Evans, 2003]. Differences in clouds are hypothesized to contribute additional radiative forcing, although the radiative effect that they had is difficult to constrain, given our lack of understanding of cloud radiative feedbacks and uncertainties regarding the precision of data from this time period [Goldblatt and Zahnle, 2011] [Charnay et al., 2020]. With the idea that clouds respond to radiative forcing perturbations similarly for a variety of background climate states, modern observations of cloud feedbacks could then be used to constrain the radiative effect of clouds in the Archean as well. This would clarify what other components of the climate system

need to have contributed to the additional 50 W/m^2 of radiative forcing necessary to keep early Earth warm.

This work is also applicable to challenges in the study of climates on other planets, where climate parameters such as clouds, solar insolation, and greenhouse gas concentration can be drastically different from conditions on Earth. Clouds have different radiative effects for planets orbiting different types of stars, and cloud responses to radiative perturbations can strongly depend on the physical configuration of the planets on which they occur [Kitzmann et al., 2010]. In constraining the responsiveness of clouds to greenhouse gas radiative forcing for several climate states, we potentially simplify added complexities to cloud radiative feedbacks on other planets.

Finally, findings of this study are also applicable to studies in solar geoengineering, a science centered on reducing the severity of modern climate change impacts by injecting reflective aerosols into the atmosphere [Irvine et al., 2016] [Kravitz et al., 2011] [MacMartin et al., 2014] [Irvine et al., 2016] [MacMartin et al., 2018]. Variation of the solar constant, as done in this study, is effectively identical to this process; indeed, similar experimentation has been done in the Geoengineering Model Intercomparison Project (GeoMIP) [Kravitz et al., 2011]. The work done in this study may compliment the physical science basis developed in literature on this subject and further justify the benefits and drawbacks of using solar geoengineering to mitigate anthropogenic climate change.

Bibliography

- H. Abdul-Razzak and S. J. Ghan. A parameterization of aerosol activation: 2. Multiple aerosol types. *Journal of Geophysical Research: Atmospheres*, 105(D5):6837–6844, 2000. ISSN 2156-2202. doi: 10.1029/1999JD901161. URL <https://onlinelibrary.wiley.com/doi/abs/10.1029/1999JD901161>. eprint: <https://onlinelibrary.wiley.com/doi/pdf/10.1029/1999JD901161>.
- B. A. Albrecht. Aerosols, Cloud Microphysics, and Fractional Cloudiness. *Science*, 245(4923):1227–1230, 1989. ISSN 0036-8075. URL <http://www.jstor.org/stable/1704234>. Publisher: American Association for the Advancement of Science.
- F. A.-M. Bender, V. Ramanathan, and G. Tselioudis. Changes in extratropical storm track cloudiness 1983–2008: observational support for a poleward shift. *Climate Dynamics*, 38(9):2037–2053, May 2012. ISSN 1432-0894. doi: 10.1007/s00382-011-1065-6. URL <https://doi.org/10.1007/s00382-011-1065-6>.
- A. K. Betts and Harshvardhan. Thermodynamic constraint on the cloud liquid water feedback in climate models. *Journal of Geophysical Research: Atmospheres*, 92(D7):8483–8485, 1987. ISSN 2156-2202. doi: 10.1029/JD092iD07p08483. URL <https://onlinelibrary.wiley.com/doi/abs/10.1029/JD092iD07p08483>. eprint: <https://onlinelibrary.wiley.com/doi/pdf/10.1029/JD092iD07p08483>.
- R. Bintanja and F. M. Selten. Future increases in Arctic precipitation linked to local evaporation and sea-ice retreat. *Nature*, 509(7501):479–482, May 2014. ISSN 1476-4687. doi: 10.1038/nature13259. URL <https://www.nature.com/articles/nature13259>. Number: 7501 Publisher: Nature Publishing Group.
- J. Bjordal, T. Storelvmo, K. Alterskjær, and T. Carlsen. Equilibrium climate sensitivity above 5 °C plausible due to state-dependent cloud feedback. *Nature Geoscience*, 13(11):718–721, Nov. 2020. ISSN 1752-0908. doi: 10.1038/s41561-020-00649-1.

- URL <https://www.nature.com/articles/s41561-020-00649-1>. Number: 11
 Publisher: Nature Publishing Group.
- J.-L. Brenguier, H. Pawlowska, L. Schüller, R. Preusker, J. Fischer, and Y. Fouquart. Radiative Properties of Boundary Layer Clouds: Droplet Effective Radius versus Number Concentration. *Journal of the Atmospheric Sciences*, 57(6):803–821, Mar. 2000. ISSN 0022-4928, 1520-0469. doi: 10.1175/1520-0469(2000)057<0803:RPOBLC>2.0.CO;2. URL https://journals.ametsoc.org/view/journals/atsc/57/6/1520-0469_2000_057_0803_rpoblc_2.0.co_2.xml. Publisher: American Meteorological Society Section: Journal of the Atmospheric Sciences.
- B. Byrne and C. Goldblatt. Radiative forcing at high concentrations of well-mixed greenhouse gases. *Geophysical Research Letters*, 41(1):152–160, 2014. ISSN 1944-8007. doi: 10.1002/2013GL058456. URL <https://onlinelibrary.wiley.com/doi/abs/10.1002/2013GL058456>. eprint: <https://onlinelibrary.wiley.com/doi/pdf/10.1002/2013GL058456>.
- R. Caballero and M. Huber. State-dependent climate sensitivity in past warm climates and its implications for future climate projections. *Proceedings of the National Academy of Sciences*, 110(35):14162–14167, Aug. 2013. doi: 10.1073/pnas.1303365110. URL <https://www.pnas.org/doi/full/10.1073/pnas.1303365110>. Publisher: Proceedings of the National Academy of Sciences.
- P. Ceppi, F. Brant, M. D. Zelinka, and D. L. Hartmann. Cloud feedback mechanisms and their representation in global climate models. *WIREs Climate Change*, 8(4):e465, 2017. ISSN 1757-7799. doi: 10.1002/wcc.465. URL <https://onlinelibrary.wiley.com/doi/abs/10.1002/wcc.465>. eprint: <https://onlinelibrary.wiley.com/doi/pdf/10.1002/wcc.465>.
- L. H. Chambers, B. Lin, and D. F. Young. Examination of New CERES Data for Evidence of Tropical Iris Feedback. *Journal of Climate*, 15(24):3719–3726, Dec. 2002. ISSN 0894-8755, 1520-0442. doi: 10.1175/1520-0442(2002)015<3719:EONCDF>2.0.CO;2. URL https://journals.ametsoc.org/view/journals/clim/15/24/1520-0442_2002_015_3719_eoncdf_2.0.co_2.xml. Publisher: American Meteorological Society Section: Journal of Climate.

- B. Charnay, F. Forget, R. Wordsworth, J. Leconte, E. Millour, F. Codron, and A. Spiga. Exploring the faint young Sun problem and the possible climates of the Archean Earth with a 3-D GCM: A 3-D MODELING OF THE CLIMATES OF THE ARCHEAN EARTH. *Journal of Geophysical Research: Atmospheres*, 118(18):10,414–10,431, Sept. 2013. ISSN 2169897X. doi: 10.1002/jgrd.50808. URL <http://doi.wiley.com/10.1002/jgrd.50808>.
- B. Charnay, E. T. Wolf, B. Marty, and F. Forget. Is the Faint Young Sun Problem for Earth Solved? *Space Science Reviews*, 216(5):90, July 2020. ISSN 1572-9672. doi: 10.1007/s11214-020-00711-9. URL <https://doi.org/10.1007/s11214-020-00711-9>.
- M. Collins, S.-I. An, W. Cai, A. Ganachaud, E. Guilyardi, F.-F. Jin, M. Jochum, M. Lengaigne, S. Power, A. Timmermann, G. Vecchi, and A. Wittenberg. The impact of global warming on the tropical Pacific Ocean and El Niño. *Nature Geoscience*, 3(6):391–397, June 2010. ISSN 1752-0908. doi: 10.1038/ngeo868. URL <https://www.nature.com/articles/ngeo868>. Number: 6 Publisher: Nature Publishing Group.
- D. A. D. Evans. A fundamental Precambrian–Phanerozoic shift in earth’s glacial style? *Tectonophysics*, 375(1):353–385, Nov. 2003. ISSN 0040-1951. doi: 10.1016/S0040-1951(03)00345-7. URL <https://www.sciencedirect.com/science/article/pii/S0040195103003457>.
- N. Feldl and S. Bordoni. Characterizing the Hadley Circulation Response through Regional Climate Feedbacks. *Journal of Climate*, 29(2):613–622, Jan. 2016. ISSN 0894-8755, 1520-0442. doi: 10.1175/JCLI-D-15-0424.1. URL <https://journals.ametsoc.org/view/journals/clim/29/2/jcli-d-15-0424.1.xml>. Publisher: American Meteorological Society Section: Journal of Climate.
- G. Flato, J. Marotzke, B. Abiodun, P. Braconnot, S. C. Chou, W. Collins, P. Cox, F. Driouech, S. Emori, V. Eyring, et al. Evaluation of climate models. In *Climate change 2013: the physical science basis. Contribution of Working Group I to the Fifth Assessment Report of the Intergovernmental Panel on Climate Change*, pages 741–866. Cambridge University Press, 2014.
- G. Gastineau, H. L. Treut, and L. Li. Hadley circulation changes under global warming conditions indicated by coupled climate models. *Tellus A: Dynamic Meteorology and Oceanography*, 63(1):1–12, 2011. doi: 10.1111/j.1600-0854.2010.00502.x. URL <https://doi.org/10.1111/j.1600-0854.2010.00502.x>.

- orology and Oceanography*, 60(5):863–884, Jan. 2008. ISSN null. doi: 10.1111/j.1600-0870.2008.00344.x. URL <https://doi.org/10.1111/j.1600-0870.2008.00344.x>. Publisher: Taylor & Francis eprint: <https://doi.org/10.1111/j.1600-0870.2008.00344.x>.
- A. Gettelman and S. C. Sherwood. Processes Responsible for Cloud Feedback. *Current Climate Change Reports*, 2(4):179–189, Dec. 2016. ISSN 2198-6061. doi: 10.1007/s40641-016-0052-8. URL <https://doi.org/10.1007/s40641-016-0052-8>.
- M. Godolt, J. L. Grenfell, D. Kitzmann, M. Kunze, U. Langematz, A. B. C. Patzer, H. Rauer, and B. Stracke. Assessing the habitability of planets with Earth-like atmospheres with 1D and 3D climate modeling. *Astronomy & Astrophysics*, 592:A36, Aug. 2016. ISSN 0004-6361, 1432-0746. doi: 10.1051/0004-6361/201628413. URL <https://www.aanda.org/articles/aa/abs/2016/08/aa28413-16/aa28413-16.html>. Publisher: EDP Sciences.
- C. Goldblatt and K. J. Zahnle. Clouds and the Faint Young Sun Paradox. *Climate of the Past*, 7(1):203–220, Mar. 2011. ISSN 1814-9332. doi: 10.5194/cp-7-203-2011. URL <http://arxiv.org/abs/1102.3209>. arXiv: 1102.3209.
- C. Goldblatt, V. L. McDonald, and K. E. McCusker. Earth’s long-term climate stabilized by clouds. *Nature Geoscience*, 14(3):143–150, Mar. 2021. ISSN 1752-0894, 1752-0908. doi: 10.1038/s41561-021-00691-7. URL <http://www.nature.com/articles/s41561-021-00691-7>.
- N. M. J. Hall, B. J. Hoskins, P. J. Valdes, and C. A. Senior. Storm tracks in a high-resolution GCM with doubled carbon dioxide. *Quarterly Journal of the Royal Meteorological Society*, 120(519):1209–1230, 1994. ISSN 1477-870X. doi: 10.1002/qj.49712051905. URL <https://onlinelibrary.wiley.com/doi/abs/10.1002/qj.49712051905>. eprint: <https://onlinelibrary.wiley.com/doi/pdf/10.1002/qj.49712051905>.
- J. Hansen, M. Sato, G. Russell, and P. Kharecha. Climate sensitivity, sea level and atmospheric carbon dioxide. *Philosophical Transactions of the Royal Society A: Mathematical, Physical and Engineering Sciences*, 371(2001):20120294, Oct. 2013. doi: 10.1098/rsta.2012.0294. URL <https://royalsocietypublishing.org/doi/full/10.1098/rsta.2012.0294>. Publisher: Royal Society.

- D. L. Hartmann and M. L. Michelsen. NO EVIDENCE FOR IRIS. *Bulletin of the American Meteorological Society*, 83(2):249–254, Feb. 2002. ISSN 0003-0007, 1520-0477. doi: 10.1175/1520-0477(2002)083<0249:NEFI>2.3.CO;2. URL https://journals.ametsoc.org/view/journals/bams/83/2/1520-0477_2002_083_0249_nefi_2_3_co_2.xml. Publisher: American Meteorological Society Section: Bulletin of the American Meteorological Society.
- I. M. Held and B. J. Soden. Robust Responses of the Hydrological Cycle to Global Warming. *Journal of Climate*, 19(21):5686–5699, Nov. 2006. ISSN 0894-8755, 1520-0442. doi: 10.1175/JCLI3990.1. URL <https://journals.ametsoc.org/view/journals/clim/19/21/jcli3990.1.xml>. Publisher: American Meteorological Society Section: Journal of Climate.
- P. Huang and J. Ying. A Multimodel Ensemble Regression Method to Correct the Tropical Pacific SST Change Patterns under Global Warming. *Journal of Climate*, 28(12):4706–4723, June 2015. ISSN 0894-8755, 1520-0442. doi: 10.1175/JCLI-D-14-00833.1. URL <https://journals.ametsoc.org/view/journals/clim/28/12/jcli-d-14-00833.1.xml>. Publisher: American Meteorological Society Section: Journal of Climate.
- P. J. Irvine, B. Kravitz, M. G. Lawrence, and H. Muri. An overview of the Earth system science of solar geoengineering. *WIREs Climate Change*, 7(6):815–833, 2016. ISSN 1757-7799. doi: 10.1002/wcc.423. URL <https://onlinelibrary.wiley.com/doi/abs/10.1002/wcc.423>. eprint: <https://onlinelibrary.wiley.com/doi/pdf/10.1002/wcc.423>.
- G. S. Jenkins. A general circulation model study of the effects of faster rotation rate, enhanced CO₂ concentration, and reduced solar forcing: Implications for the faint young sun paradox. *Journal of Geophysical Research: Atmospheres*, 98(D11):20803–20811, 1993. ISSN 2156-2202. doi: 10.1029/93JD02056. URL <https://agupubs.onlinelibrary.wiley.com/doi/abs/10.1029/93JD02056>.
- J. E. Kay and A. Gettelman. Cloud influence on and response to seasonal Arctic sea ice loss. *Journal of Geophysical Research: Atmospheres*, 114(D18), 2009. ISSN 2156-2202. doi: 10.1029/2009JD011773. URL <https://onlinelibrary.wiley.com/doi/abs/10.1029/2009JD011773>. eprint: <https://onlinelibrary.wiley.com/doi/pdf/10.1029/2009JD011773>.

- D. Kitzmann, A. B. C. Patzer, P. v. Paris, M. Godolt, B. Stracke, S. Gebauer, J. L. Grenfell, and H. Rauer. Clouds in the atmospheres of extrasolar planets - I. Climatic effects of multi-layered clouds for Earth-like planets and implications for habitable zones. *Astronomy & Astrophysics*, 511:A66, Feb. 2010. ISSN 0004-6361, 1432-0746. doi: 10.1051/0004-6361/200913491. URL <https://www.aanda.org/articles/aa/abs/2010/03/aa13491-09/aa13491-09.html>. Publisher: EDP Sciences.
- B. Kravitz, A. Robock, O. Boucher, H. Schmidt, K. E. Taylor, G. Stenchikov, and M. Schulz. The Geoengineering Model Intercomparison Project (GeoMIP). *Atmospheric Science Letters*, 12(2):162–167, 2011. ISSN 1530-261X. doi: 10.1002/asl.316. URL <https://onlinelibrary.wiley.com/doi/abs/10.1002/asl.316>. eprint: <https://onlinelibrary.wiley.com/doi/pdf/10.1002/asl.316>.
- W. K. M. Lau and K.-M. Kim. Robust Hadley Circulation changes and increasing global dryness due to CO₂ warming from CMIP5 model projections. *Proceedings of the National Academy of Sciences*, 112(12):3630–3635, Mar. 2015. doi: 10.1073/pnas.1418682112. URL <https://www.pnas.org/doi/abs/10.1073/pnas.1418682112>. Publisher: Proceedings of the National Academy of Sciences.
- M. G. Lawrence. The Relationship between Relative Humidity and the Dewpoint Temperature in Moist Air: A Simple Conversion and Applications. *Bulletin of the American Meteorological Society*, 86(2):225–234, Feb. 2005. ISSN 0003-0007, 1520-0477. doi: 10.1175/BAMS-86-2-225. URL <https://journals.ametsoc.org/view/journals/bams/86/2/bams-86-2-225.xml>. Publisher: American Meteorological Society Section: Bulletin of the American Meteorological Society.
- G. Le Hir, Y. Teitler, F. Fluteau, Y. Donnadieu, and P. Philippot. The faint young Sun problem revisited with a 3-D climate–carbon model – Part 1. *Climate of the Past*, 10(2):697–713, Apr. 2014. ISSN 1814-9332. doi: 10.5194/cp-10-697-2014. URL <https://www.clim-past.net/10/697/2014/>.
- R. S. Lindzen, M.-D. Chou, and A. Y. Hou. Does the Earth Have an Adaptive Infrared Iris? *Bulletin of the American Meteorological Society*, 82(3):417–432, Mar. 2001. ISSN 0003-0007, 1520-0477. doi: 10.1175/1520-0477(2001)082<0417:DTEHAA>2.3.CO;2. URL https://journals.ametsoc.org/view/journals/bams/82/3/1520-0477_2001_082_0417_dtehaha_2_3_co_2.xml. Publisher: American Meteorological Society Section: Bulletin of the American Meteorological Society.

- D. G. MacMartin, K. Caldeira, and D. W. Keith. Solar geoengineering to limit the rate of temperature change. *Philosophical Transactions of the Royal Society A: Mathematical, Physical and Engineering Sciences*, 372(2031):20140134, Dec. 2014. doi: 10.1098/rsta.2014.0134. URL <https://royalsocietypublishing.org/doi/full/10.1098/rsta.2014.0134>. Publisher: Royal Society.
- D. G. MacMartin, K. L. Ricke, and D. W. Keith. Solar geoengineering as part of an overall strategy for meeting the 1.5°C Paris target. *Philosophical Transactions of the Royal Society A: Mathematical, Physical and Engineering Sciences*, 376(2119):20160454, May 2018. doi: 10.1098/rsta.2016.0454. URL <https://royalsocietypublishing.org/doi/full/10.1098/rsta.2016.0454>. Publisher: Royal Society.
- S. Manabe and R. T. Wetherald. The Effects of Doubling the CO₂ Concentration on the climate of a General Circulation Model. *Journal of the Atmospheric Sciences*, 32(1):3–15, Jan. 1975. ISSN 0022-4928, 1520-0469. doi: 10.1175/1520-0469(1975)032<0003:TEODTC>2.0.CO;2. URL https://journals.ametsoc.org/view/journals/atsc/32/1/1520-0469_1975_032_0003_teodtc_2_0_co_2.xml. Publisher: American Meteorological Society Section: Journal of the Atmospheric Sciences.
- C. Mbengue and T. Schneider. Storm Track Shifts under Climate Change: What Can Be Learned from Large-Scale Dry Dynamics. *Journal of Climate*, 26(24):9923–9930, Dec. 2013. ISSN 0894-8755, 1520-0442. doi: 10.1175/JCLI-D-13-00404.1. URL <https://journals.ametsoc.org/view/journals/clim/26/24/jcli-d-13-00404.1.xml>. Publisher: American Meteorological Society Section: Journal of Climate.
- E. A. Middlemas, A. C. Clement, B. Medeiros, and B. Kirtman. Cloud Radiative Feedbacks and El Niño–Southern Oscillation. *Journal of Climate*, 32(15):4661–4680, Aug. 2019. ISSN 0894-8755, 1520-0442. doi: 10.1175/JCLI-D-18-0842.1. URL <https://journals.ametsoc.org/view/journals/clim/32/15/jcli-d-18-0842.1.xml>. Publisher: American Meteorological Society Section: Journal of Climate.
- E. A. Middlemas, J. E. Kay, B. M. Medeiros, and E. A. Maroon. Quantifying the Influence of Cloud Radiative Feedbacks on Arctic Surface Warming Using

- Cloud Locking in an Earth System Model. *Geophysical Research Letters*, 47(15):e2020GL089207, 2020. ISSN 1944-8007. doi: 10.1029/2020GL089207. URL <https://onlinelibrary.wiley.com/doi/abs/10.1029/2020GL089207>. eprint: <https://onlinelibrary.wiley.com/doi/pdf/10.1029/2020GL089207>.
- T. Owen, R. D. Cess, and V. Ramanathan. Enhanced CO₂ greenhouse to compensate for reduced solar luminosity on early Earth. *Nature*, 277(5698):640–642, Feb. 1979. ISSN 1476-4687. doi: 10.1038/277640a0. URL <https://www.nature.com/articles/277640a0>. Number: 5698 Publisher: Nature Publishing Group.
- R. Rondanelli and R. S. Lindzen. Can thin cirrus clouds in the tropics provide a solution to the faint young Sun paradox? *Journal of Geophysical Research: Atmospheres*, 115(D2), 2010. ISSN 2156-2202. doi: 10.1029/2009JD012050. URL <https://agupubs.onlinelibrary.wiley.com/doi/abs/10.1029/2009JD012050>.
- B. E. J. Rose. Lecture13 – Heat transport, 2015. URL https://www.atmos.albany.edu/facstaff/brose/classes/ATM623_Spring2015/Notes/Lectures/Lecture13%20-%20Heat%20transport.html#section7.
- M. T. Rosing, D. K. Bird, N. H. Sleep, and C. J. Bjerrum. No climate paradox under the faint early Sun. *Nature*, 464(7289):744–747, Apr. 2010. ISSN 1476-4687. doi: 10.1038/nature08955. URL <https://www.nature.com/articles/nature08955>. Number: 7289 Publisher: Nature Publishing Group.
- R. Rye, P. H. Kuo, and H. D. Holland. Atmospheric carbon dioxide concentrations before 2.2 billion years ago. *Nature*, 378(6557):603–605, Dec. 1995. ISSN 1476-4687. doi: 10.1038/378603a0. URL <https://www.nature.com/articles/378603a0>. Number: 6557 Publisher: Nature Publishing Group.
- C. Sagan and G. Mullen. Earth and Mars: Evolution of Atmospheres and Surface Temperatures. *Science*, 177(4043):52–56, July 1972. doi: 10.1126/science.177.4043.52. URL <https://www-science-org.ezproxy.library.uvic.ca/doi/10.1126/science.177.4043.52>. Publisher: American Association for the Advancement of Science.
- N. D. Sheldon. Precambrian paleosols and atmospheric CO₂ levels. *Precambrian Research*, 147(1):148–155, June 2006. ISSN 0301-9268. doi: 10.1016/j.precamres.2006.02.004. URL <https://www.sciencedirect.com/science/article/pii/S0301926806000581>.

- H. K. A. Singh, C. M. Bitz, A. Donohoe, and P. J. Rasch. A Source–Receptor Perspective on the Polar Hydrologic Cycle: Sources, Seasonality, and Arctic–Antarctic Parity in the Hydrologic Cycle Response to CO₂ Doubling. *Journal of Climate*, 30(24):9999–10017, Dec. 2017. ISSN 0894-8755, 1520-0442. doi: 10.1175/JCLI-D-16-0917.1. URL <https://journals.ametsoc.org/view/journals/clim/30/24/jcli-d-16-0917.1.xml>. Publisher: American Meteorological Society Section: Journal of Climate.
- G. L. Stephens. Cloud Feedbacks in the Climate System: A Critical Review. *Journal of Climate*, 18(2):237–273, Jan. 2005. ISSN 0894-8755, 1520-0442. doi: 10.1175/JCLI-3243.1. URL <https://journals.ametsoc.org/view/journals/clim/18/2/jcli-3243.1.xml>. Publisher: American Meteorological Society Section: Journal of Climate.
- G. L. Stephens, S.-C. Tsay, P. W. Stackhouse, and P. J. Flatau. The Relevance of the Microphysical and Radiative Properties of Cirrus Clouds to Climate and Climatic Feedback. *Journal of the Atmospheric Sciences*, 47(14):1742–1754, July 1990. ISSN 0022-4928, 1520-0469. doi: 10.1175/1520-0469(1990)047<1742:TROTMA>2.0.CO;2. URL https://journals.ametsoc.org/view/journals/atsc/47/14/1520-0469_1990_047_1742_trotma_2_0_co_2.xml. Publisher: American Meteorological Society Section: Journal of the Atmospheric Sciences.
- Z. Sun and K. P. Shine. Studies of the radiative properties of ice and mixed-phase clouds. *Quarterly Journal of the Royal Meteorological Society*, 120(515):111–137, 1994. ISSN 1477-870X. doi: 10.1002/qj.49712051508. URL <https://onlinelibrary.wiley.com/doi/abs/10.1002/qj.49712051508>. eprint: <https://onlinelibrary.wiley.com/doi/pdf/10.1002/qj.49712051508>.
- G. A. Vecchi and B. J. Soden. Global Warming and the Weakening of the Tropical Circulation. *Journal of Climate*, 20(17):4316–4340, Sept. 2007. ISSN 0894-8755, 1520-0442. doi: 10.1175/JCLI4258.1. URL <https://journals.ametsoc.org/view/journals/clim/20/17/jcli4258.1.xml>. Publisher: American Meteorological Society Section: Journal of Climate.
- A. S. von der Heydt and P. Ashwin. State dependence of climate sensitivity: attractor constraints and palaeoclimate regimes. *Dynamics and Statistics of the Climate System*, 1(1):dzx001, Jan. 2016. ISSN 2059-6987. doi: 10.1093/climsys/dzx001. URL <https://doi.org/10.1093/climsys/dzx001>.

- R. T. Wetherald and S. Manabe. Cloud Feedback Processes in a General Circulation Model. *Journal of the Atmospheric Sciences*, 45(8):1397–1416, Apr. 1988. ISSN 0022-4928, 1520-0469. doi: 10.1175/1520-0469(1988)045<1397:CFPIAG>2.0.CO;2. URL https://journals.ametsoc.org/view/journals/atsc/45/8/1520-0469_1988_045_1397_cfpiag_2_0_co_2.xml. Publisher: American Meteorological Society Section: Journal of the Atmospheric Sciences.
- E. Wolf and O. Toon. Hospitable Archean Climates Simulated by a General Circulation Model. *Astrobiology*, 13(7):656–673, July 2013. ISSN 1531-1074, 1557-8070. doi: 10.1089/ast.2012.0936. URL <http://www.liebertpub.com/doi/10.1089/ast.2012.0936>.
- R. Wood and C. S. Bretherton. On the Relationship between Stratiform Low Cloud Cover and Lower-Tropospheric Stability. *Journal of Climate*, 19(24):6425–6432, Dec. 2006. ISSN 0894-8755, 1520-0442. doi: 10.1175/JCLI3988.1. URL <https://journals.ametsoc.org/view/journals/clim/19/24/jcli3988.1.xml>. Publisher: American Meteorological Society Section: Journal of Climate.
- J. Ying, P. Huang, and R. Huang. Evaluating the formation mechanisms of the equatorial Pacific SST warming pattern in CMIP5 models. *Advances in Atmospheric Sciences*, 33(4):433–441, Apr. 2016. ISSN 1861-9533. doi: 10.1007/s00376-015-5184-6. URL <https://doi.org/10.1007/s00376-015-5184-6>.
- M. Yoshimori, T. Yokohata, and A. Abe-Ouchi. A Comparison of Climate Feedback Strength between CO₂ Doubling and LGM Experiments. *Journal of Climate*, 22(12):3374–3395, June 2009. ISSN 0894-8755, 1520-0442. doi: 10.1175/2009JCLI2801.1. URL <https://journals.ametsoc.org/view/journals/clim/22/12/2009jcli2801.1.xml>. Publisher: American Meteorological Society Section: Journal of Climate.
- M. D. Zelinka, S. A. Klein, and D. L. Hartmann. Computing and Partitioning Cloud Feedbacks Using Cloud Property Histograms. Part I: Cloud Radiative Kernels. *Journal of Climate*, 25(11):3715–3735, June 2012. ISSN 0894-8755, 1520-0442. doi: 10.1175/JCLI-D-11-00248.1. URL <http://journals.ametsoc.org/doi/10.1175/JCLI-D-11-00248.1>.
- X.-T. Zheng, S.-P. Xie, L.-H. Lv, and Z.-Q. Zhou. Intermodel Uncertainty in ENSO Amplitude Change Tied to Pacific Ocean Warming Pattern. *Journal of*

Climate, 29(20):7265–7279, Oct. 2016. ISSN 0894-8755, 1520-0442. doi: 10.1175/JCLI-D-16-0039.1. URL <https://journals.ametsoc.org/view/journals/clim/29/20/jcli-d-16-0039.1.xml>. Publisher: American Meteorological Society Section: Journal of Climate.